


**THE DESIGN AND CONSTRUCTION
OF A DISCRIMINATING ČERENKOV
VETO COUNTER ARRAY**

by

Gregory James Trayling
B.Sc., Simon Fraser University, 1991.

A thesis submitted in partial fulfillment
of the requirements for the degree of
Master of Science
in the Department
of Physics and Astronomy.

We accept this thesis as conforming
to the required standard.


Dr. G. R. Mason, Physics Department, University of Victoria


Dr. A. Olin, Physics Department, University of Victoria


Dr. C. E. Picciotto, Physics Department, University of Victoria


Dr. T. E. Gough, Chemistry Department, University of Victoria


Dr. J. A. Macdonald, External Examiner, TRIUMF

© Gregory James Trayling, 1994,
University of Victoria.

*All rights reserved. Thesis may not be reproduced in whole or in part,
by photocopy or other means, without the permission of the author.*

QC 490.4
T7

Co-Supervisors: Dr. A. Olin, Dr. G. R. Mason.

Abstract

The development and use of a water Čerenkov detector array as a discriminating veto counter for an experiment involving the measurement of the K-series kaonic hydrogen X-rays is discussed. The techniques devised for manufacturing a number of identical detectors are presented, along with specific details of both a prototype and the final array of sixteen units. Results of efficiency tests performed on both designs are displayed.

Examiners:

[Redacted]

✓ Dr. G. R. Mason, Physics Department, University of Victoria

[Redacted]

Dr. A. Olin, Physics Department, University of Victoria

[Redacted]

Dr. C. E. Picciotto, Physics Department, University of Victoria

[Redacted]

Dr. T. E. Gough, Chemistry Department, University of Victoria

[Redacted]

Dr. J. A. Macdonald, External Examiner, TRIUMF

Acknowledgments

Many thanks to Elizabeth van der Kamp, who assisted with the Čerenkov counter construction as a co-operative education student, and to Chris Stevens and Steve Chan for their industry in the Triumph detector machine shop. Thanks also to Dr. Art Olin, Dr. Gren Mason, and Dr. David Gill for the opportunity to continue my work, and to Dr. Iwasaki Masahiko and all the members of the KPX team in Japan for their hospitality during my time there.

Table of Contents

Abstract	ii
Acknowledgements	iii
Table of Contents	iv
List of Tables	vi
List of Figures	vii
1 Introduction	1
2 Introduction to \bar{K}-N Physics	3
2.1 Kaonic Hydrogen	3
2.2 Experimental Evidence	5
2.3 Theoretical Calculations	7
2.4 The Kaonic Hydrogen Puzzle	9
3 Overview of Experiment E228	12
3.1 The KPX Approach	12
3.2 Overview of the KPX Detectors	16
3.3 Čerenkov Veto Counters	19
4 Čerenkov Detector Design	21
4.1 Čerenkov Radiation	21
4.2 Particle Discrimination	23
4.3 Ultraviolet Enhancement	26
5 Testing of the Prototype	28
5.1 Prototype design	28
5.2 Beam Discrimination Test	30

6	Detector Fabrication Techniques	36
6.1	Strip-Heat Forming	36
6.2	Bonding Techniques	38
6.3	Phototube Mounting	41
6.4	Final Design Dimensions	43
7	Testing of the Completed Array	47
7.1	Cosmic Ray Testing	47
7.2	Efficiency Results	62
8	Concluding Remarks	71
	Bibliography	72
	Appendix: Program Listing	74

List of Tables

2.1	<i>Previous experimental results for the effect of the strong interaction on the energy level and line width of the 2p-1s transition of kaonic hydrogen.</i>	7
2.2	<i>A summary of selected determinations of the s-wave scattering parameter for kaonic hydrogen.</i>	9
3.1	<i>K⁻p⁺ reaction products.</i>	13
3.2	<i>K⁻ free decay products.</i>	14
4.1	<i>Formulation used for umbelliferone solution.</i>	26
5.1	<i>Efficiencies at other momenta.</i>	31
7.1	<i>Veto efficiency, standard deviation, and number of trials for each WC^x detector.</i>	66
7.2	<i>Sectional veto efficiency, standard deviation, and number of trials for each WC^x detector (1 to 8).</i>	68
7.3	<i>Sectional veto efficiency, standard deviation, and number of trials for each WC^x detector (9 to 16).</i>	69

List of Figures

2.1	<i>Quark line diagrams of K^- capture by hydrogen nucleus for (a) the final state $\Sigma^- \pi^+$, and (b) typical free decay.</i>	4
2.2	<i>Monte Carlo simulation of gamma emission following kaon stopping in hydrogen.....</i>	5
2.3	<i>A summary of current experimental results and theoretical predictions for the energy shift and width of the 2p-1s transition of kaonic hydrogen.</i>	10
3.1	<i>Charged pion emission per $K^- p^+$ reaction (yield=1.44).....</i>	14
3.2	<i>The KPX detector array (right) and the hydrogen target (center).</i>	16
3.3	<i>A cutaway view of the detector array with the target in place.....</i>	17
3.4	<i>Estimated KPX yield of kaonic X-rays, assuming a natural width of 500 eV and a Si(Li) resolution of 200 eV.</i>	20
4.1	<i>A Huygens construction illustrating Čerenkov wavefronts. ...</i>	23
5.1	<i>A sketch of the prototype design.</i>	29
5.2	<i>The detector was tested in two different positions. Arrows represent the beam orientation.</i>	30
5.3	<i>Efficiencies for position A.</i>	32
5.4	<i>Efficiencies for position B.</i>	33

6.1	<i>Forming a sheet about an internal mold.</i>	37
6.2	<i>Removing the mold from the form.</i>	38
6.3	<i>Final assembly of the subcomponents.</i>	39
6.4	<i>Selected details of the support assembly (Dimensions are given in millimeters).</i>	42
6.5	<i>Diagram showing the proximity of a Čerenkov counter to neighboring ones.</i>	43
6.6	<i>Top and front view details of the final design.</i>	44
6.7	<i>Side view details of the final design.</i>	45
6.8	<i>Selected details of portions of the main end cap support plate.</i>	46
7.1	<i>Histograms of Čerenkov ADC values (Detectors 1 to 4). Markers indicate the position of ADC cutoffs used in the program listed in the Appendix.</i>	49
7.2	<i>Histograms of Čerenkov ADC values (Detectors 5 to 8).</i>	50
7.3	<i>Histograms of Čerenkov ADC values (Detectors 9 to 12).</i>	51
7.4	<i>Histograms of Čerenkov ADC values (Detectors 13 to 14).</i>	52
7.5	<i>Histograms of Čerenkov TDC values (Detectors 1 to 4).</i>	53
7.6	<i>Histograms of Čerenkov TDC values (Detectors 5 to 8).</i>	54

7.7	<i>Histograms of Čerenkov TDC values (Detectors 9 to 12).</i>	55
7.8	<i>Histograms of Čerenkov TDC values (Detectors 13 to 16).</i>	56
7.9	<i>T2 TDC profile histograms (Detectors 1 to 4).</i>	57
7.10	<i>T2 TDC profile histograms (Detectors 5 to 8).</i>	58
7.11	<i>T2 TDC profile histograms (Detectors 9 to 12).</i>	59
7.12	<i>T2 TDC profile histograms (Detectors 13 to 16).</i>	60
7.13	<i>Multiplicity plots for the T2 and WČ arrays.</i>	61
7.14	<i>Hitpattern plots for the T2 and WČ arrays.</i>	63
7.15	<i>An illustration of the efficiency criteria.</i>	64
7.16	<i>Hitpatterns involved in the overall efficiency calculation.</i>	65
7.17	<i>Veto efficiency calculated for each WČ detector.</i>	65
7.18	<i>Sectional WČ veto efficiencies.</i>	67

Chapter 1

Introduction

A cylindrical array of sixteen liquid Čerenkov detectors was constructed by the author as a contribution to experiment PS-E228 (KPX), which is currently running at K.E.K.¹ Details of the fabrication techniques developed are presented as a guide to reproducing similar units.

The use of these detectors as veto counters is introduced through a discussion of the KPX approach to precisely measure the kaonic hydrogen K-series X-ray spectrum. Data in this area is currently being sought in order to resolve an apparent conflict between recent experimental evidence [1]-[3], and theoretical predictions [4]-[6]. In addressing problems with previous techniques, the KPX experiment incorporates a large detector solid angle, good energy resolution with silicon-lithium (Si(Li)) X-ray detectors, and a pressurized hydrogen gas target to provide a high X-ray yield by minimizing Stark mixing in the target. In order to reject a considerable background due to γ ray production, a tag of two charged pions due to respective hyperon production and decay is required. Čerenkov counters, which have the ability to discriminate between pions and electrons at the momenta involved, are then

¹K.E.K. is the Japanese National High-Energy Physics Laboratory.

used to veto false tags caused by e^+e^- pairs resulting from high energy γ conversion.

The detector's ability to discriminate is reported from a test conducted at TRIUMF² on a prototype closely resembling the final design. Measurements on the efficiency of the completed array are presented from data acquired during a preliminary run at K.E.K.

The main conclusion is that the relative ease of manufacturing an array of identical Čerenkov detectors, using the plastic forming and bonding techniques presented, along with their high efficiency and adaptability in situations requiring particle discrimination, merits consideration of this approach in the design of any similar experiment.

²TRIUMF is the Canadian National Meson Laboratory.

Chapter 2

Introduction to \bar{K} -N Physics

2.1 Kaonic Hydrogen

The orbital electron of a hydrogen atom may be replaced by a negatively charged kaon, forming an atomic species known as kaonic hydrogen. X-rays are emitted as the K^- cascades downward to lower atomic levels, eventually to either decay weakly or react with the nucleus via the strong interaction. Examples of such processes are shown in Figure 2.1. The X-ray energy levels due to the electromagnetic interaction will be altered by the increasing presence of the strong interaction at lower orbital states. A precise measurement of these levels and their broadened spectral line widths provides data such as the S-wave scattering length for the \bar{K} -N system, a parameter which can otherwise only be determined by an arguable extrapolation from low energy scattering experiments.

Since the kaon mass is roughly 966 times that of an electron, the Bohr radii of the corresponding kaon orbitals are proportionally smaller, resulting in K-series X-rays ranging on the order of 6.5 keV for the unshifted K_α (2p-1s) transition, and up to 9 keV for higher K-series emissions. Although the precise influence of the strong interaction is unknown, it is expected to only be detectable by its effect on the lowest energy state due to the short range nature of the strong interaction and the finite density of the s-wave function at the

nucleus. Therefore, the energy differences between the K-series lines should remain unaltered since the initial states are relatively unaffected. Although this would seem to provide a good signature for their identification, assignments so far have been tentative, even for the K_α line due to poor statistics and high background.

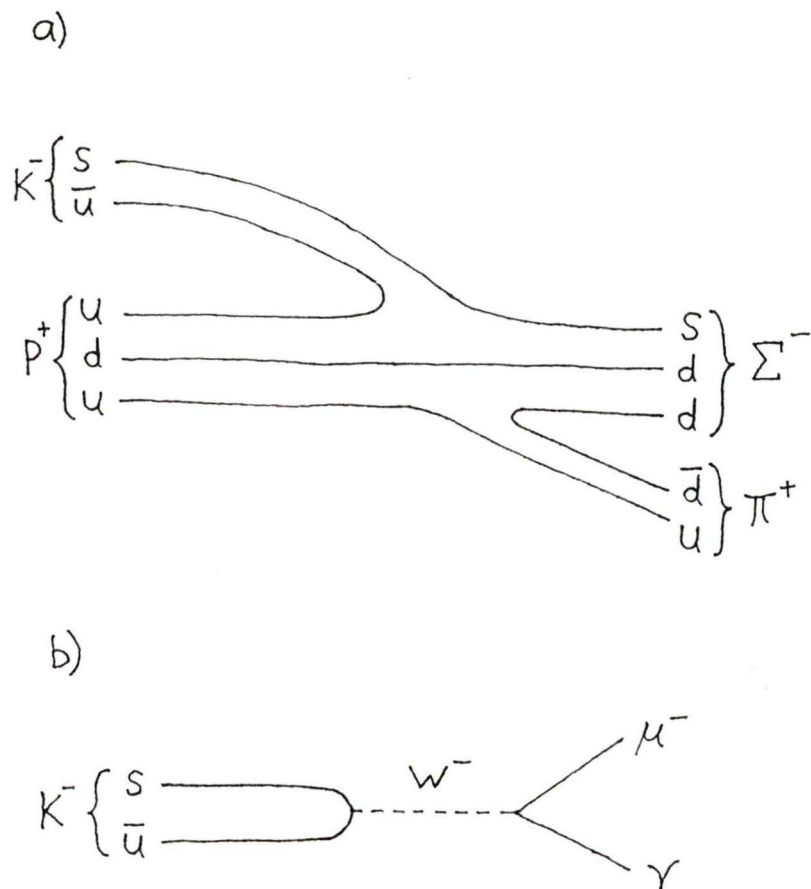


Figure 2.1 Quark line diagrams of K^- capture by hydrogen nucleus for (a) the final state $\Sigma^- \pi^+$, and (b) typical free decay.

One of the factors inhibiting the intensity of the K_α line is the strong absorption of the kaons from high level atomic s-states into nuclei. Strong electric fields arising during collisions between electrically neutral kaonic hydrogen atoms and surrounding hydrogen nuclei cause mixing of higher L-levels with s-states of the kaons (Stark effects)[7].

2.2 Experimental Evidence

The observation of X-rays from kaonic hydrogen proves to be exceptionally difficult due to the problems in producing a high intensity beam of short-lived kaons, and to the contamination of background radiation at the energies of interest. Figure 2.2 shows a Monte Carlo simulation¹ of the γ -ray emissions

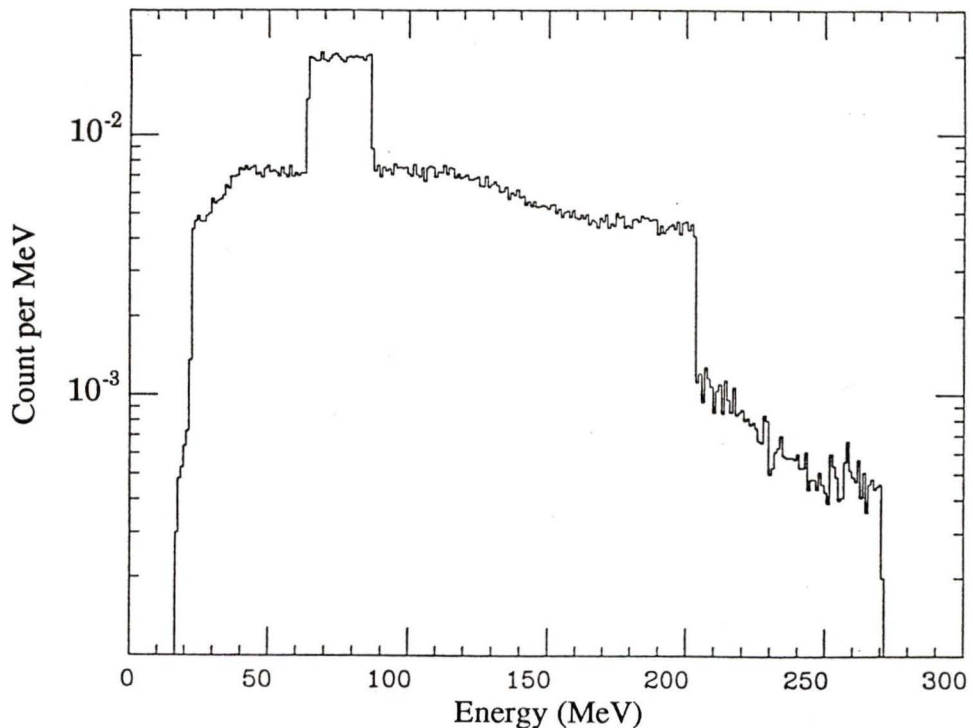


Figure 2.2: Monte Carlo Simulation of gamma emission following kaon stopping in hydrogen.

¹All Monte Carlo simulations shown were produced by the Tokyo KPX group.

expected per K^-p^+ reaction, with each reaction producing an average of 1.40 γ emissions. The structure in the spectrum is a result of several channels available to the reaction. The γ -rays tend to react with the materials surrounding the target, producing, through a variety of processes, X-rays which overwhelm the already feeble kaonic X-ray signals.

Three experiments performed to date have had only marginal success in identifying kaonic hydrogen spectra. The first of these, reported by Davies *et al* [1], observed a peak matching the unshifted energy of the 2p-1s X-rays from the K^-p^+ atom. The experiment employed a 600 MeV/c kaon beam from NIMROD (U.K.), stopping in a liquid hydrogen target, with the X-rays measured by a single Si(Li) detector with an effective area of 300 mm² and a resolution of 310 eV. Unfortunately, data acquisition was halted, due to the closure of NIMROD, before sufficient events could be gathered.

A somewhat more sophisticated experiment was subsequently performed at the low-momentum K19 beamline of CERN-PS by Izycki *et al* [2], again stopping in a liquid hydrogen target. The number of Si(Li) detectors was increased to five, each of 80 mm² detection area and 350 eV energy resolution. The results, as shown in Table 2.1, were not in agreement with those of Davies *et al*.

In an attempt to resolve this discrepancy, the apparatus used for the initial experiment was transferred to CERN-PS. In this most recent test, performed in 1982 by Bird *et al* [3], several possible candidates for kaonic hydrogen X-rays were identified, but there was only marginal agreement with the results of Izycki *et al*.

Clearly, what is needed at this point is a definitive experiment which addresses the problems encountered in the previous three by invoking higher statistics and a technique for reducing the background levels.

Table 2.1: Previous experimental results for the effect of the strong interaction on the energy level and line width of the 2p-1s transition of kaonic hydrogen.

Experiment	Shift ϵ (eV)	Line Width Γ (eV)
Davies <i>et al</i> [1].	40 ± 60	$0 +230$
Izycki <i>et al</i> [2]	270 ± 80	560 ± 260
Bird <i>et al</i> [3]	193 ± 60	80^{+220}_{-80}

2.3 Theoretical Calculations

The energy shift (ϵ) and width (Γ) of the 2p-1s X-ray may be related to the complex s-wave scattering length (a_s) [8], which, to first order in ($\mu\alpha_s$) is given by

$$\epsilon + i\Gamma/2 = 2\mu^2\alpha^3 a_s \quad (2.1)$$

where α is the fine-structure constant and μ is the reduced mass of the system. As s-wave scattering is dominant in the low momenta regime (≤ 300 MeV/c), one may use data from this region to determine the \bar{K} -N scattering lengths by using the k-matrix approach of R.H. Dalitz and S.F. Tuan [9].

The data used for the \bar{K} -N interaction at low energies consists of the K^-p^+ scattering cross sections for the elastic and inelastic ($\pi\Sigma$ and $\pi\Lambda$) channels, the branching ratios of the inelastic channels at the K^-p^+ threshold (1432 MeV), and the invariant mass distribution for $\pi\Sigma$ below this threshold. The assumption made is that k-matrix elements are smooth functions of energy, and indeed it appeared that the scattering cross section data, available down to within roughly 8 MeV above the K^-p^+ threshold, could be continuously linked to the latter two sources. This premise was strengthened when the $\Lambda(1405)$ resonance was later observed, whose existence as a quasibound state is implied by the negative value of the real part of the scattering length in the zero isospin channel.

These scattering lengths for isospin 0 and 1 were calculated by Y.-A. Chao *et al.* to be [10]

$$\begin{aligned} a_0 &= (-1.60 + i0.75) \text{ fm} \\ a_1 &= (0.08 + i0.69) \text{ fm} \end{aligned} \tag{2.2}$$

Thus, the resulting K^-p^+ scattering length should be

$$a_{kp} = \frac{1}{2}(a_0 + a_1) = (-0.76 + i0.72) \text{ fm} \tag{2.3}$$

In a somewhat more sophisticated approach, A.D. Martin [4] performed a multichannel dispersion relation analysis of the low energy data, including extrapolations from higher energies (1500 MeV) of data on the Coulomb-nuclear interference in K^-p^+ scattering. Once again, a negative real part for the total scattering length was found, similar to calculations done concurrently by R.H. Dalitz and J.G. McGinley [5]. The results of both calculations are shown in Table 2.2.

With the advent of refined bubble chamber studies of neutral hyperon production in K^-p^+ reactions of low momentum, it was discovered that there is a significant contribution to the channels possible from p-wave interactions in the $\Lambda\pi^0$ sector at momenta <200 MeV/c. This afforded calculations, performed by J.E. Conboy *et al.* [6], of the \bar{K} -N scattering lengths which differed considerably from the previous two. However, all three agreed that the resulting energy shift in the kaonic hydrogen 2p-1s X-ray line should be negative, implying a repulsive contribution from the strong interaction.

Table 2.2: A summary of selected determinations of the s-wave scattering parameter for kaonic hydrogen.

Method	Originators	a_{Kp} (fm)
Kaonic X-rays	Davies et al. [1]	$(0.10 \pm 0.15) + i(0.00 \pm 0.28)$
	Izycki et al. [2]	$(0.65 \pm 0.19) + i(0.68 \pm 0.31)$
	Bird et al. [3]	$(0.47 \pm 0.14) + i(0.10^{+0.27}_{-0.10})$
\bar{K} -N Scattering analysis	Chao et al. [10]	$-0.76 + i0.72$
	Martin et al. [4]	$-0.66 + i0.64$
	Dalitz et al. [5]	$-0.73 + i0.63$
	Conboy et al. [6]	$-0.045 + i0.84$

2.4 The Kaonic Hydrogen Puzzle

The sign discrepancy between the theoretical and experimental results for a_{Kp} has since become known as the "kaonic hydrogen puzzle", and is the prime motivation for more precise experiments, along with many attempts to modify existing theory.

It was first suggested that there exists an aberrant Coulomb correction to the scattering length a_{Kp} [11]. A more favoured approach, advanced by K.S Kumar and Y.Nogami [12], postulates an unseen elementary baryon Λ_0 , with a mass near the K^-p^+ threshold, and whose quantum numbers are identical to that of the $\Lambda(1405)$ resonance. The presence of such a Λ_0 particle would rescind the continuous extrapolations performed in previous calculations, and thus avoid the apparent paradox of the kaonic hydrogen puzzle by producing rapid variations in scattering amplitudes near this threshold. The original Kumar-Nogami model was later broadened by K. Tanaka and A. Suzuki [13], including all relevant channels and considering fits to a more extensive set of

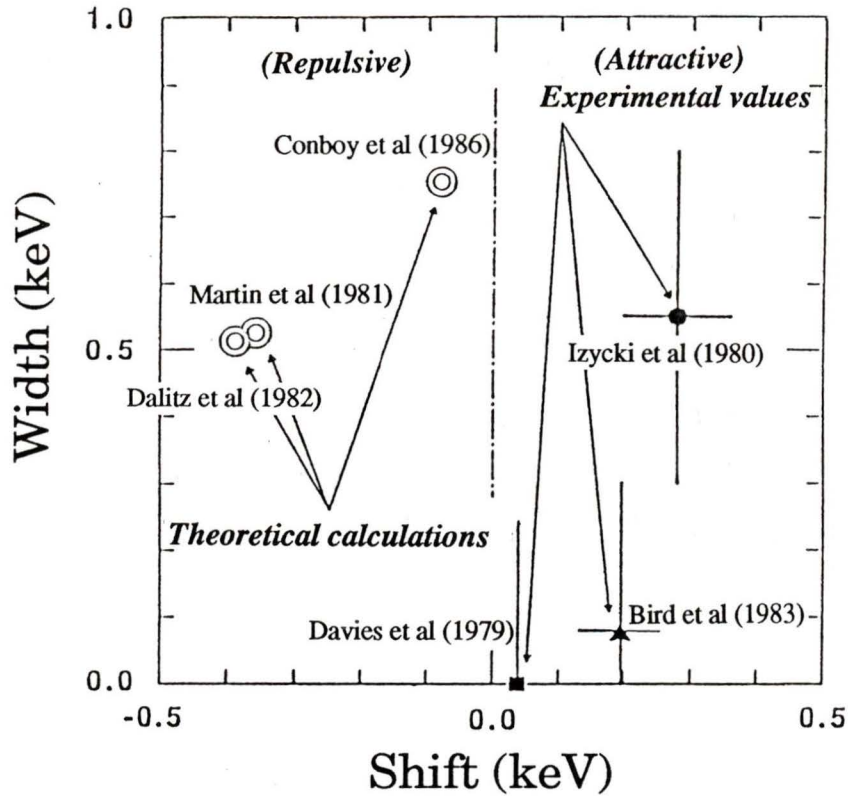


Figure 2.3: A summary of current experimental results and theoretical predictions for the energy shift and width of the 2p-1s transition of kaonic hydrogen.

data, such as the branching ratios at threshold. However, this approach was found to be lacking in its predictions for inelastic processes.

A third set of theories was initiated by J. Schnick and R.H. Landau [14] which renewed the interpretation of the $\Lambda(1405)$ as being a two-body system. By applying relativistic kinematics in a coupled channel mode, they were able to obtain a positive real part in the K^-p^+ scattering length by fitting the low momentum scattering data with no need for anomalous corrections near threshold energies. Tanaka and Suzuki also extended this approach [13] in the same manner as the Kumar-Nogami model, and found that, although the full relativistic corrections are not required, the more comprehensive treatment can

encompass all existing data, including the kaonic hydrogen shift. However, the same calculations can be made disregarding the kaonic atom data, resulting in a set of parameters which still need to be determined by experiment. If the scattering amplitude of K^-p^+ contains further anomalies, it may be necessary to introduce the Λ_0 into this model as well.

The correct interpretation of the $\Lambda(1405)$ resonance is a point of controversy which will hopefully be resolved by further experiments. It is not clear whether the $\Lambda(1405)$ is a \bar{K} -N bound state, a $\pi\Sigma$ resonance, a three quark state, or possibly some combination of these. The model most successful in predicting accurate measurements of the kaonic hydrogen K-series spectrum will dictate the $\Lambda(1405)$ structure through its effect on the scattering length..

Chapter 3

Overview of Experiment E228

3.1 The KPX Approach

In order to escape the deluge of background X-rays, and thus achieve a higher signal-to-noise ratio, one is lead to consider specific interactions devoid of γ production. Table 3.1 summarizes the main products possible from K^-p^+ reactions. The first column presents the intermediate products, followed by the final produced particles. (The Σ and Λ are both very short-lived and not directly detectable in this experiment.) It is immediately apparent that by only observing events with a pion yield of 2, that is, by filtering out all but the first two reactions, the γ -ray contamination will be substantially reduced. Further restrictions using vertex information limit the reactions to those originating from within the hydrogen gas target.

Reactions such as $K^0n \rightarrow \pi^+\pi^-n$, where K^0n is produced by charge exchange, need not be tabulated since their threshold is above the energy available from the stopped K^-p^+ system. The cross sections for this reaction as the K^- is slowing down are so small as to be safely neglected.

Consider Figure 3.1, which displays a Monte Carlo simulation of the π^+ momenta distribution resulting from the reactions of Table 3.1. The two narrow peaks are due to the monoenergetic pions emitted during Σ^\pm production

Table 3.1: $K^- p^+$ reaction products.

Reaction ($K^- p^+ \rightarrow$ Intermediate \rightarrow Final)	Branching Ratio	$\pi/\mu/e > 150 \text{ MeV}/c$ Yield
$\Sigma^- \pi^+ \rightarrow \pi^+ \pi^- n$	46%	2
$\Sigma^+ \pi^- \rightarrow \pi^- \pi^+ n$	10%	2
$\Sigma^0 \pi^0 \rightarrow \pi^- p^+ 3\gamma$	18%	0
$\Sigma^+ \pi^- \rightarrow \pi^- p^+ 2\gamma$	10%	1
$\Sigma^0 \pi^0 \rightarrow n 5\gamma$	10%	0
$\Lambda \pi^0 \rightarrow \pi^- p^+ 2\gamma$	4%	0
$\Lambda \pi^0 \rightarrow n 4\gamma$	2%	0

at the primary vertex, with the more intense of the two peaks attributed to the slightly more massive Σ^- . The remaining pion momenta arise from the subsequent weak decays of the hyperons produced, which are no longer monoenergetic due to the various pion emission geometries possible. It is interesting that one may completely disregard false 2π triggers arising from coincidences involving Λ decay by invoking a momentum cut at 150 MeV/c.

The restriction of π^\pm yield=2 and $p_\pi > 150 \text{ MeV}/c$ has further utility when one considers the products from free kaon decay, as listed in Table 3.2, which are all vetoed under such a selection. Also filtered out are the production of γ -rays by π^- charge exchange and absorption in hydrogen (Panovski γ), which do not produce two triggers. This method of $2\pi^\pm$ tagging for stopped kaons has an efficiency of only 0.28; however, this is far offset by subsequent reductions in background.

The reduction in background X-rays may be further assisted by removing all high Z ($Z > 13$) materials from the detector area. For example, the K_α (6.404 keV) and K_β (7.058 keV) electronic X-ray lines are very close to the expected kaonic proton K-series peaks; hence, iron should not be used in the target area. Aluminum is a favoured material, with a characteristic electronic

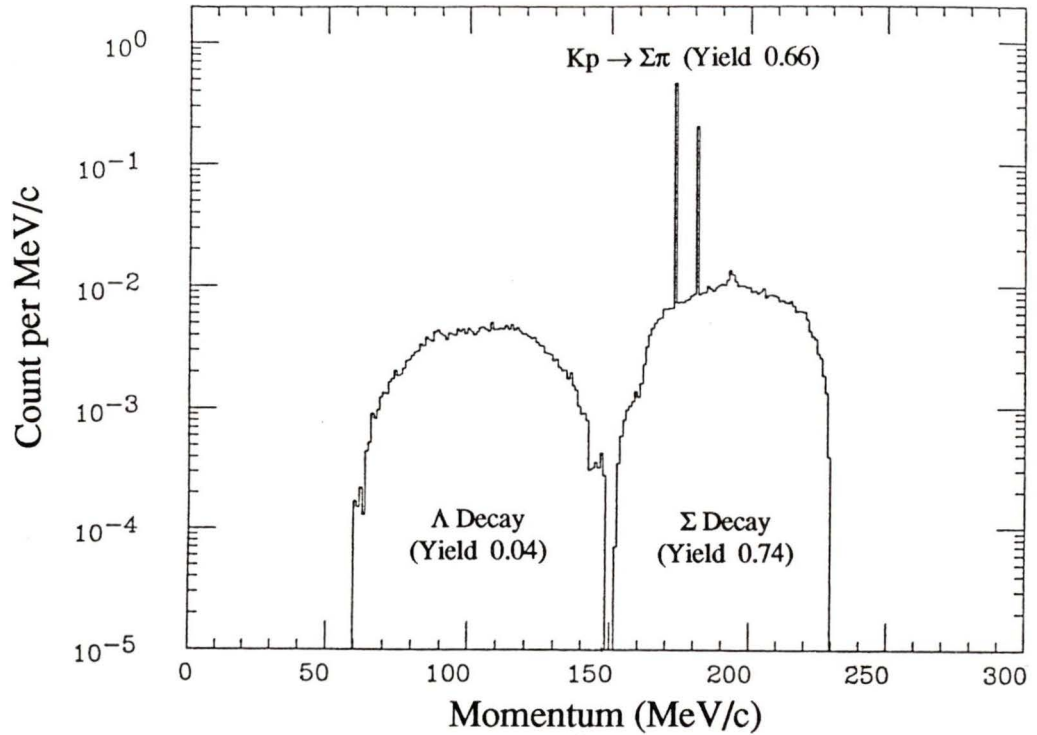


Figure 3.1: Charged pion emission per $K^- p^+$ reaction (yield=1.44).

Table 3.2: K^- free decay products.

Reaction (Intermediate \rightarrow Final)	Branching Ratio	$\pi/\mu/e > 150$ MeV/c Yield
$\mu^- \nu$	63.5%	1
$\pi^- \pi^0 \rightarrow \pi^- 2\gamma$	21.2%	1
$\pi^- \pi^- \pi^+ \rightarrow \pi^- 4\gamma$	5.59%	0
$e^- \pi^0 \nu \rightarrow e^- 2\gamma$	4.82%	1
$\mu^- \pi^0 \nu \rightarrow \mu^- 2\gamma$	3.18%	1
$\pi^- \pi^0 \pi^0 \rightarrow \pi^- 4\gamma$	1.73%	0

K_{α} X-ray peak near 1.4 keV. Although there are several high level kaonic transitions in aluminum, $8 \rightarrow 7$ at 7.0 keV for example, which are near the kaonic hydrogen K_{α} X-ray line, it is believed that the intensities are sufficiently low that they can be suppressed by using vertex information from the detector array to narrow the data acceptance to within the hydrogen. An alternative would be to coat critical areas with a layer of carbon or beryllium, neither of which would produce contaminating spectra.

Another improvement of the KPX approach is an enhancement of the K_{α} X-ray yield per stopped kaon. Previous experiments have all used liquid hydrogen (equivalent in density to 700 atm at room temperature) in an attempt to maximize the K^{-} stopping ratio, which one would expect to be proportional to the hydrogen density. However, Stark mixing also becomes stronger in denser media, whereby a kaon in both a high energy and high angular momentum state is affected by ambient electric fields, allowing the kaon to mix with lower l-states and be directly captured by the nucleus. One may use known data on the Stark mixing of protons in hydrogen to select an optimum target density. In the KPX experiment, hydrogen gas at 4 atm and 77K (equivalent in density to 15 atm at room temperature) was chosen, resulting in an estimated two orders of magnitude improvement in the K_{α} X-ray yield per stopped kaon. Using gas in place of liquid also allows an enlargement of the target area volume to a few liters, which is favorable for increasing the number of stopped kaons.

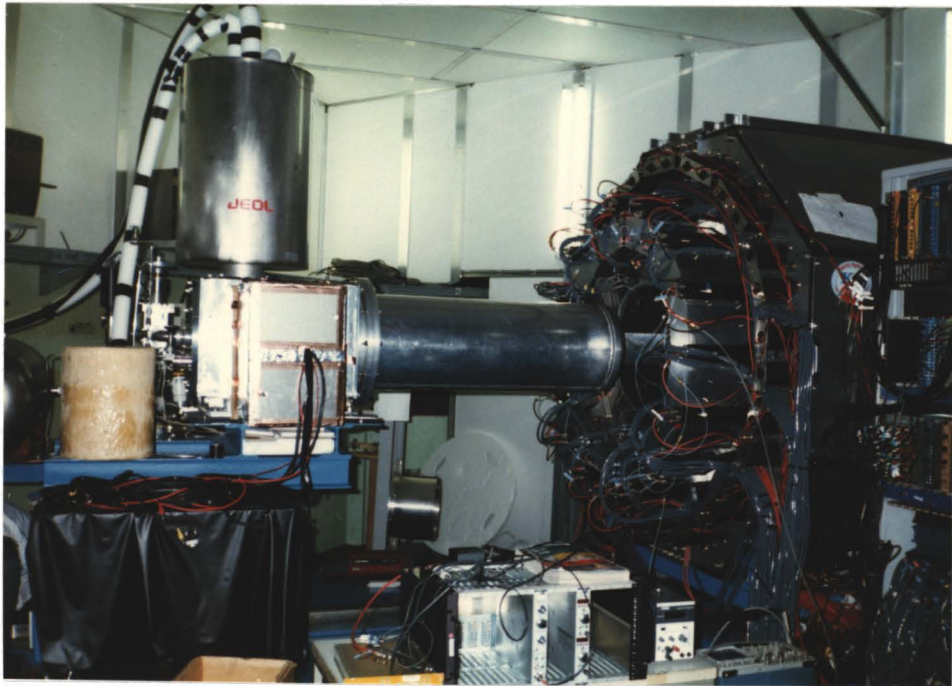


Figure 3.2: The KPK detector array (right) and the hydrogen target (center).

3.2 Overview of the KPX Detectors

In the KPX setup, an incident beam of $600 \text{ MeV}/c \text{ K}^-$ particles from the K3 production target is passed through a d.c. separator to reduce the accompanying pion flux to a level comparable to that of the kaons. The beam then passes through a beam defining counter system consisting of a time-of-flight (TOF) starting counter inside the beamline, and then to an arrangement of plastic scintillators and acrylic Čerenkov counters located within the experiment area. This enables the identification of kaon and pion pulses. The beam is then degraded just prior to the target using carbon blocks in order to maximize the ratio of stopped kaons to the kaon beam flux in the target, with essentially all of the beam pions passing through the target unstopped. The kaon stopping ratio has been estimated at 1.4×10^{-3} , resulting in a stopped kaon yield per pulse on the order of 100. The K_α X-ray yield per

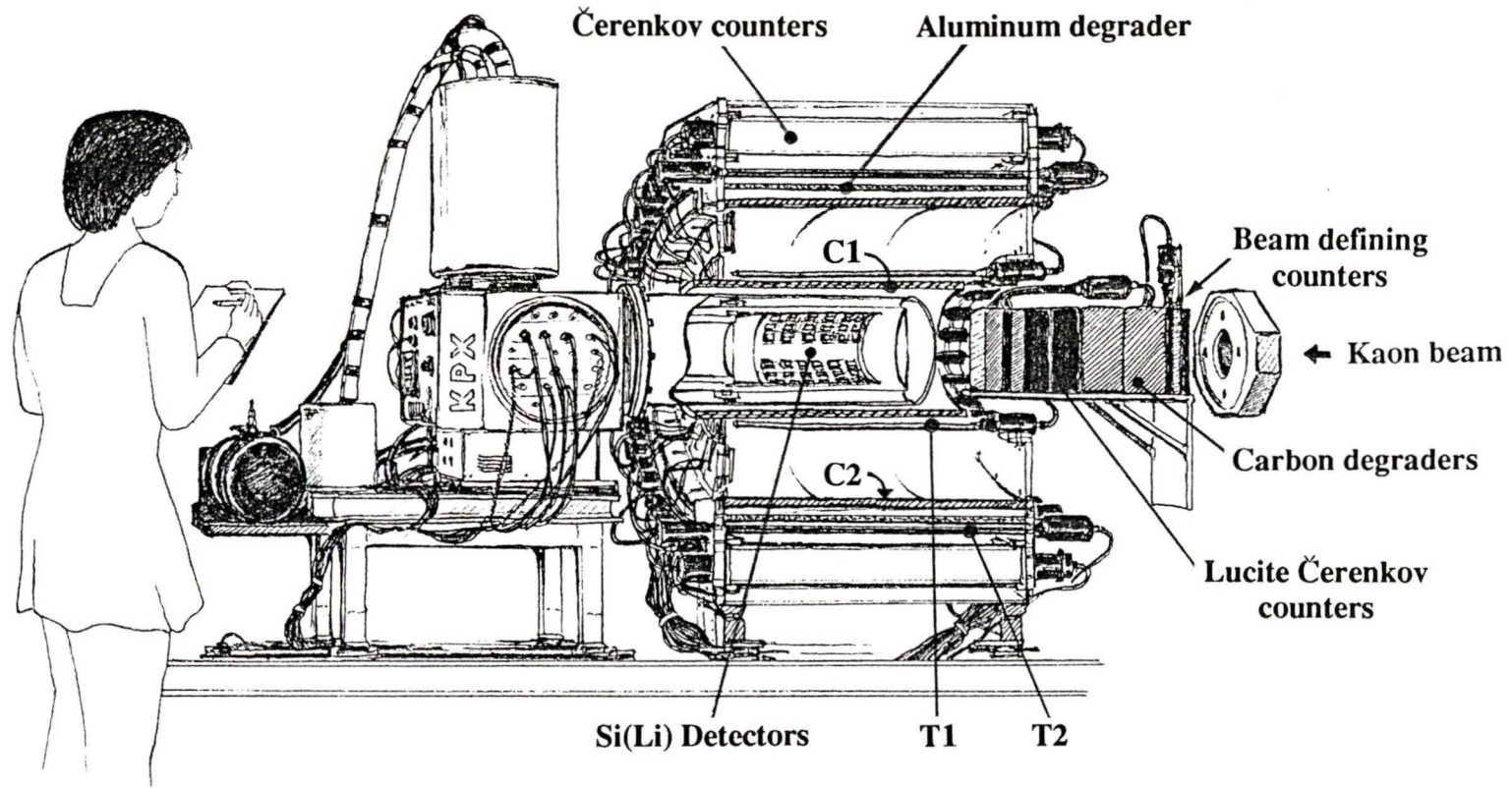


Figure 3.3: A cutaway view of the detector array with the target in place.

stopped K^- has been further estimated at 6×10^{-3} . The target, shown withdrawn from the detectors in Figure 3.2, contains gaseous hydrogen at up to 4 atm, cooled by a thin layer of liquid nitrogen.

On the inner surface of the target chamber is an array of 60 solid-state Si(Li) X-ray detectors. Each detector has a surface area of 200 mm^2 , which in total encompasses a fractional solid angle of 0.048 about the center of the target, an increase in a factor of 100 over that of any previous experiment. An interesting feature of the KPX plan is that the Si(Li) detectors are immersed within the hydrogen target, thus eliminating the need for windows, which attenuate X-rays and give a bias to the energy spectra. Current experimental runs indicate that the resolution will be as low as 350 eV (full width at half maximum), although some problems are presented by the pion halo of the beam, which deposits energy within the detectors and affects the reset electronics. The reset rate is expected to result in not more than a 6% data loss due to coincidental X-ray hits in the array.

Immediately surrounding the target vessel is the first of two multiwire proportional chambers (MWPC), labelled C1 and C2 in Figure 3.3. Both were originally constructed for the ASTERIX spectrometer at LEAR, but have now been equipped with specially designed pre-amplifier boards for the KPX experiment. Each chamber consists of a tubular array of hundreds of high potential anode wires, surrounded on both sides at a gap by two sheets containing cathode strips which wind in opposing helical patterns, thus allowing one to locate the position and direction of a traversing particle which ionizes the intermediate gas. These MWPC chambers allow vertex reconstruction in order to apply cuts restricting the data acceptance to events triggered from within the target area, greatly reducing the noise from spurious events originating in the surrounding apparatus. C1 and C2 have cylindrical projection angles of 35° and 45° respectively, yielding a 70% coverage of the total solid angle for target emissions.

Surrounding the inner wire chamber is an axial array of 16 plastic scintillator counters (T1). These provide time-of-flight information when taken in tandem with a similar set (T2) located outside C2. Limited tracking of particles is also possible along the length of T2 by analyzing the time delay difference between phototubes coupled to both ends of the scintillators. Inside the T2 array is a set of parallel aluminum degraders, which serve to absorb protons prior to triggering T2. Pions and leptons experience only a small energy loss due to its installation.

3.3 Čerenkov Veto Counters

A major source of false triggers for the $2\pi^\pm$ scheme is the abundance of photoelectrons resulting from high energy γ conversion and π^0 decay occurring throughout the apparatus. To remedy this, the entire detector array is sided with a cylindrical set of sixteen water Čerenkov detectors to veto such events. High energy photoelectrons are all relativistic and trigger Čerenkov radiation within the counters. The comparatively slower pions are still relativistic, but traverse the detectors at a velocity which is near or below the threshold for detection. One may then veto data acquisition for the occurrence of photoelectrons, tolerating a small percentage of false vetoes for pions which may occasionally trigger the array.

The entire experimental procedure is anticipated to result in a signal-to-noise ratio 4 orders of magnitude greater than previous experiments, with a 1 order of magnitude improvement in the statistics due to high beam intensity and increased kaon stopping yield. An early Monte Carlo simulation of the expected results is shown in Figure 3.4, although it is somewhat optimistic with an estimated K_α X-ray count of 2800 and a Si(Li) resolution of 200eV (FWHM).

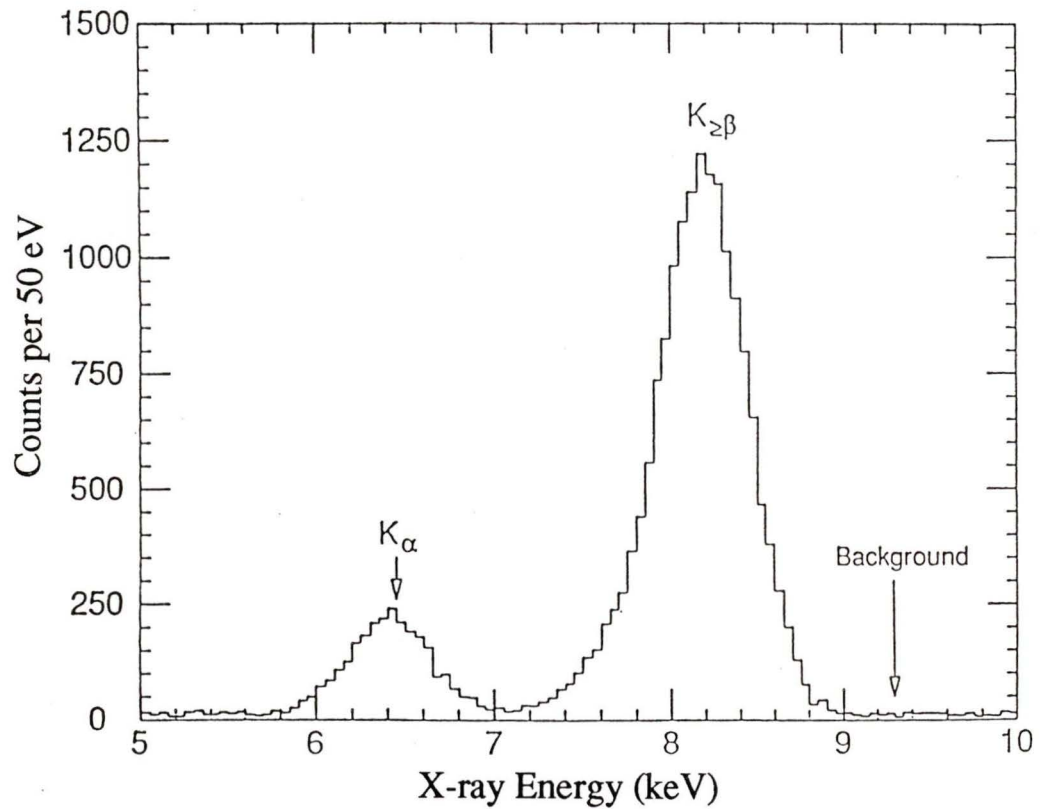


Figure 3.4: Estimated KPX yield of kaonic X-rays, assuming a natural width of 500 eV and a Si(Li) resolution of 200 eV.

Chapter 4

Čerenkov Detector Design

4.1 Čerenkov Radiation

Blue light emitted from transparent substances in the presence of radioactive sources had been observed by several individuals, most notably L. Mallet [15], but was not thoroughly investigated until P.A. Čerenkov [16] undertook a series of experiments to uncover the underlying principle. A theory presented concurrently by I.M. Frank and Ig. Tamm [17] provided a classical model of this effect for any charged particle traversing a medium with a velocity exceeding that of light in the that medium. According to this theory, electromagnetic radiation is emitted as a result of the time varying electric dipole moment created by the asymmetric polarization of the medium about the particle along its direction of travel.

Consider such a particle of mass m and relativistic momentum $\gamma m\mathbf{v}$ passing through a material of dielectric constant $\epsilon = \epsilon_1 + i\epsilon_2$, emitting a photon of energy $\hbar\omega$ and momentum $\hbar\mathbf{k}$. The four-momentum of the particle after emission (P_f) is related to that of the photon (P_γ) and that of the particle before emission (P_i) by

$$P_f = P_i - P_\gamma \quad (4.1)$$

Taking the scalar product of each side of (4.1) with itself yields

$$(2P_i - P_\gamma) \cdot P_\gamma = 0 \quad (4.2)$$

in the limit that the trajectory of the particle remains unaltered. The effective mass of the photon (P_γ^2) in the medium may be neglected, and then

$$\omega = \mathbf{v} \cdot \mathbf{k} = vk \cos \theta_c \quad (4.3)$$

where ω is the angular frequency of the photon, and θ_c is the angle between \mathbf{k} , the wavevector of the outgoing photon, and \mathbf{v} , the velocity of the particle.

The energy and momentum of a photon in the medium are bound by the dispersion relation

$$\omega^2 = \frac{k^2 c^2}{\epsilon} \quad (4.4)$$

In the optical region, where photon energies are much smaller than the excitation energies of the medium, ϵ is real, therefore Equations (4.3) and (4.4) yield

$$\cos \theta_c = \frac{1}{\beta n} \quad (4.5)$$

where $n = \sqrt{\epsilon_1} = \sqrt{\epsilon}$ is the refractive index of the medium and β is the reduced velocity of the particle. Equation (4.5) is known as the "Čerenkov relation", and describes a continuum of cones about the particle track, upon which real photons may be emitted, known as Čerenkov radiation. Note that for real θ_c , $\beta \geq 1/n$ must be satisfied. Hence, no emissions occur for particle velocities less than $\beta_c = 1/n$, the Čerenkov velocity threshold.

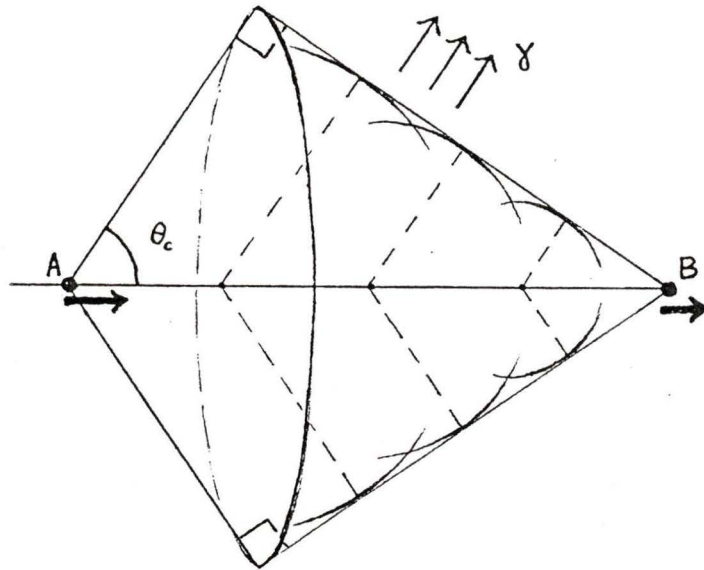


Figure 4.1: A Huygens construction illustrating Čerenkov wavefronts.

In a more elementary derivation, one may also interpret this radiation as arising from a plane wave front formed by the coherence of wavelets from all portions of the charged particle's trajectory, as illustrated in the Huygens construction of Figure 4.1. Such a geometry is possible if the velocity of the particle exceeds the phase velocity of light in the medium (c/n), from which Equation (4.5) immediately follows. Thus, the quantum mechanical description of a photon emitted at point A in Figure 4.1 also has the classical interpretation of resulting from a conical shock wave of the same particle at point B.

4.2 Particle Discrimination

Apart from being able to determine the velocity of a known charged particle from a measurement of θ_c , one may also invoke the lack of Čerenkov radiation below the velocity threshold to discriminate between particles with the same momentum but differing masses.

The Čerenkov threshold for a particle of mass m and momentum \mathbf{p} may be equated to a threshold refractive index as

$$n_c = 1/\beta_c = \sqrt{1 + m^2 c^2 / p^2} \quad (4.6)$$

Therefore one may discriminate between two particles of differing threshold refractive indices n_1 and n_2 by choosing a medium with a value of n intermediate between the these two indices.

One may deduce in a semi-classical argument [17] that the number of Čerenkov photons emitted in the wavelength range $\lambda_1 \leq \lambda \leq \lambda_2$ along a track of length $L \gg \lambda$ is given by

$$N = 2\pi\alpha L \int_{\lambda_2}^{\lambda_1} \sin^2\theta_c \mathcal{J} \lambda^2 d\lambda \quad (4.7)$$

$(\beta n > 1)$

where α is the fine-structure constant ($\alpha \approx 1/137$). As N increases with increasing θ_c , it would then be favorable to choose the intermediate value of n close to that of the slower of the two particles in order to maximize the photon count for the faster one. Incidentally, Equation (4.7) does not imply an infinite radiation output, since in practice a medium is always dispersive, restricting Čerenkov radiation to wavelengths for which $n(\lambda) > 1/\beta$. Typically, transparent media exhibit peak values of n in the near-ultraviolet, with broad bands in the visible and far-infrared..

In the KPX experiment, pions of momenta in the range of roughly 150 MeV/c to 230 MeV/c should not cause Čerenkov radiation in the veto array. With an estimated momentum loss of 10% due to the presence of aluminum degraders prior to the Čerenkov counters, this corresponds to a value of $n=1.21$ for the upper momentum bound. This n value would certainly allow

the vetoing of any relativistic electron false triggers, which would be detectable down to roughly 0.75 MeV/c. Unfortunately, there are no common materials with a refractive index close to this value. Anticipating that only a fraction of the photons generated will actually be detected, one may compromise by selecting a slightly higher value of n , and tolerating a small percentage of false vetos. Water is a natural choice at $n=1.33$, with most other transparent liquids having slightly higher n values.

A rough estimate of a detector's performance may be made by assuming a constant value of n over the spectral sensitivity range. Choosing a particle track length of approximately 10 cm, phototubes which detect in the visible range ($400 \text{ nm} < \lambda < 700 \text{ nm}$) with an average quantum yield of roughly 20% and occupy a total of 3% of the internal surface area (as in the final design), a value of $N=5$ is obtained from Equation (4.7) for a pion at the maximum momentum after degradation of 207 MeV/c. The threshold of one photon count in such a case is 166 MeV/c. An electron ($\beta \approx 1$), on the other hand, will consistently generate 12 detectable photons. Appropriate threshold settings on the electronics should be able to discern between these two cases.

One point of initial concern in the design is the use of acrylic for the container walls, which have a refractive index of $n=1.48$ and occupy a volume 1/6 that of the water. Čerenkov radiation from the walls may contribute to the pion false veto rate. However, the total path length is only 10% that of the solution for tracks originating from the KPX target, yielding $N=1.0$ for upper momentum pions, and most photons generated within the walls would be absorbed in the translucent white interior.

Of less concern is transition radiation, created when a particle traverses a boundary between two media having different optical properties. This is most easily interpreted classically as arising from a varying dipole moment created by the approaching particle and its image charge in the denser medium. Such

radiation is rare with the energies and materials involved, and is typically in the X-ray region, completely outside the sensitivity of the phototubes.

4.3 Ultraviolet Enhancement

Since the number of Čerenkov photons from both the electrons and pions appear to be of the same order, it would be desirable to aid discrimination by increasing both counts by a multiplicative constant. Aside from increasing the path length L , one may extend the effective phototube sensitivity range by introducing a fluorescent agent which acts to convert some of the ultraviolet Čerenkov radiation to the visible. The wavelength shifter chosen was 4-methyl-umbelliferone [18], which has an absorption peak at 350 nm and an emission peak at 450 nm.

In order to fluoresce, this compound must be in a solution with a pH of at least 8.0. The preparation used is shown in Table 4.1. After the addition of the first two components listed, the first batch prepared was measured as $\text{pH} > 10$.

Table 4.1: Formulation used for umbelliferone solution

18.8 mL 30% $(\text{NH}_4)\text{OH}$
1.69 g $(\text{NH}_4)_2\text{HPO}_4$
10.395 mg 4-methyl-umbelliferone
18.0 L De-ionized water (Measured resistivity $> 10^7 \Omega\text{-cm}$)

This formulation has no effect on the transparency of the water and typically results in a visible light output gain of 2 to 3 over that of untreated water [11]. This is slightly higher than one would expect from a rough estimate, due to a somewhat greater value of $n \approx 1.35$ for water in the ultraviolet region. The presence of this mixture seems to inhibit biological growth, which would otherwise affect the clarity of the water. Another advantage of ultraviolet enhancement is that the mixture is not present in the acrylic, and enhancement of just the solution suppresses any relative contribution from false pion triggers originating from within the container walls.

The presence of the aluminum degraders and other apparatus interior to the Čerenkov detectors only serves to decrease the false veto rates and also trims coincidental triggers arising from lower energy Λ decays.

It should also be added that there do exist a small number of organic compounds with refractive indices within a few percent of the target value $n=1.21$. A detector could be constructed with such a material, providing one sufficiently transparent was found. Ultraviolet enhancement could be achieved by various coatings applied to the phototubes, if available wavelength shifters were found to be unstable in the chosen material.

Chapter 5

Testing of the Prototype

5.1 Prototype Design

A prototype version of a water/umbelliferone Čerenkov detector is shown in Figure 5.1; Its dimensions and phototube configuration approximated those anticipated in the final design. The goal of constructing this prototype was to investigate the discrimination efficiency of a detector whose inner walls were the natural diffuse white of the acrylic to be used. This was a favoured alternative to various schemes involving mirror-like internal surfaces. The prototype would also remove doubt as to the structural integrity of the vessel under a full load of solution.

The detector midsection was constructed by solvent bonding four sheets of 6 mm thick white acrylic, whose edges had been milled to a precise fit and held in place with small nylon bolts prior to gluing. Each end was capped with a 13 mm thick clear acrylic plate whose surface was milled such that the plate protruded 6 mm into the midsection for structural strength, leaving a 7 mm thick mounting flange. This plate was affixed by a solvent bond, covered with a 2-part epoxy fillet to prevent leaks.

Four 3" diameter phototubes were mounted inside cylindrical magnetic shields, which were in turn epoxied into two acrylic frames bolted to both ends of the main body. Pliable transparent silicone rubber disks, 6 mm in

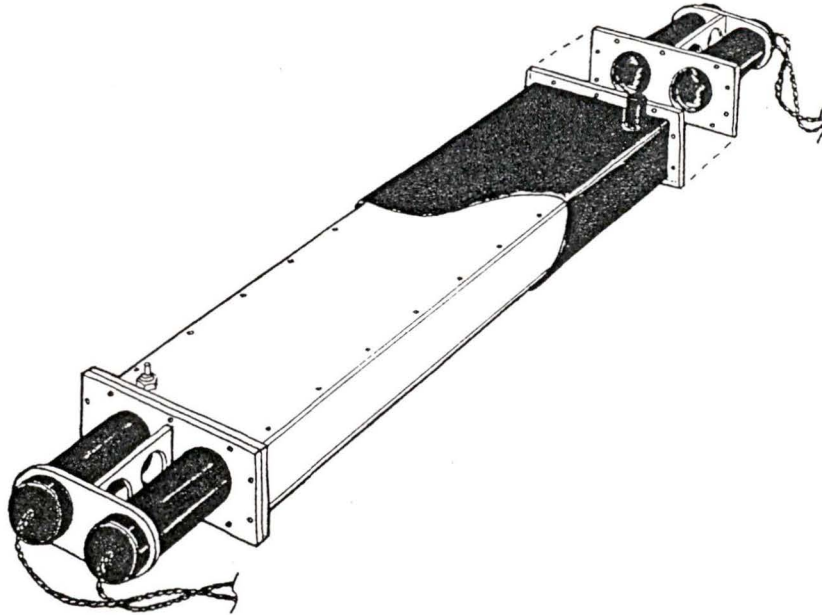


Figure 5.1: A sketch of the prototype design.

thickness, were made to fit between the phototubes and the endpieces to provide cushioning while still affording good optical contact. The ends were then wrapped in several layers of black electrical tape. During single photon counting tests, it was determined that two layers of 0.25 mm thick black vinyl sheet were required about the main body to provide isolation from ambient light. This relatively dense shielding was needed due to the large surface area involved.

The active volume of the detector was 83 mm x 248 mm x 1168 mm, filled with 24.0 L of umbelliferone solution. Two plastic valve fittings, which could be coupled to siphons, were set into opposing corners on one face. As the opaque sheeting and tape tend to draw in liquid by capillary action, the detector must be filled with care so that spilled solution is not later mistaken for structural leaks.

5.2 Beam Discrimination Test

The ability of the prototype to discriminate between electrons and pions was tested using the M13 beam line at TRIUMF. The detector was placed in one of the two positions illustrated in Figure 5.2, with the discrimination efficiency then measured for various phototube voltages. This was achieved by placing 11 cm x 13 cm x 0.6 cm plastic scintillator counters on opposite sides of the Čerenkov body, intercepting the beam axis. The outputs of these two counters and a gating pulse from the 43 ns period cyclotron RF signal were taken in coincidence, providing a count of the number of electrons or pions. The difference in the time of flight between the electrons and pions of the same momenta in the beam resulted in a 9 ns gap between their respective burst peaks at the detectors, allowing one to examine the response of the Čerenkov counter to either species by adding a suitable delay to the RF pulse. The outputs of the Čerenkov phototubes were integrated with a timing filter amplifier, whose integration time was sufficient to ensure that photons from the same event reaching different phototubes would have overlapping amplitudes. This output was then taken in coincidence with the gate for the species under consideration. The ratio of the Čerenkov count to the total

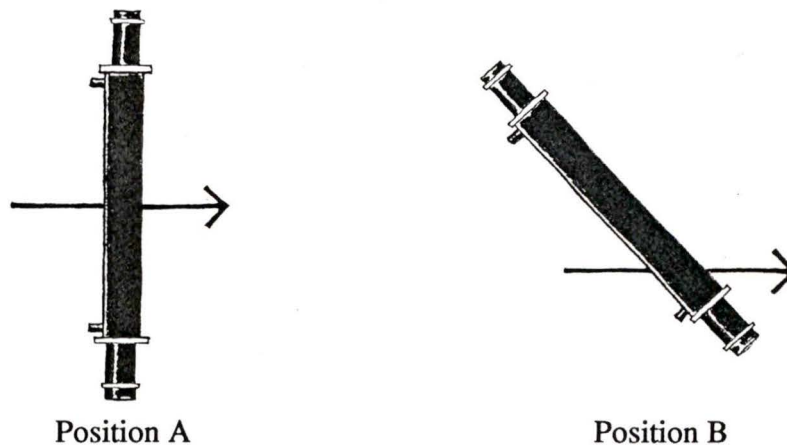


Figure 5.2: The detector was tested in two different positions. Arrows represent the beam orientation.

gated beam count for either the pions or electrons then defined the efficiency of the Čerenkov counter for that species.

In each case, the total ungated Čerenkov count during a 10 sec sampling interval was on the order of 1×10^5 , and the total count for the two beam counters in coincidence was on the order of 3.7×10^4 . The coincident beam rate for the electron and pion bursts was typically 750 per sec and 2,700 per sec respectively at 150 MeV/c. The threshold for signal over noise from the phototubes was set at 20 mV.

Tests were primarily performed at 150 MeV/c, which is actually below the pion Čerenkov threshold in water of 160 MeV/c, as there was considerable concern that the acrylic container, with a threshold of 130 MeV/c, would cause false pion triggers, especially near the phototubes.

Figure 5.3 displays the results for position A, which tests the sensitivity of the counter for tracks that are at a maximum distance from the phototubes. At around 1300 V, roughly 99% efficiency in the detection of electrons can be achieved, with less than 0.5% of pions being falsely vetoed. This was deemed to be acceptable for the proposed experiment.

Position B was used to investigate any anomalous response to tracks that were both near one pair of phototubes and roughly at the extreme of angle acceptance for the entire apparatus. As expected, Figure 5.4 shows a much higher sensitivity to both species.

Table 5.1: Efficiencies at other momenta.

Position	Beam	Momentum	Voltage	Efficiency
A	electrons	135 MeV/c	1350 V	(99.6 + 0.8) %
A	pions	135 MeV/c	1350 V	(0.16 + 0.03)%
A	pions	135 MeV/c	1300 V	(0.15 + 0.04)%
B	pions	165 MeV/c	1300 V	(5.3 + 0.3) %

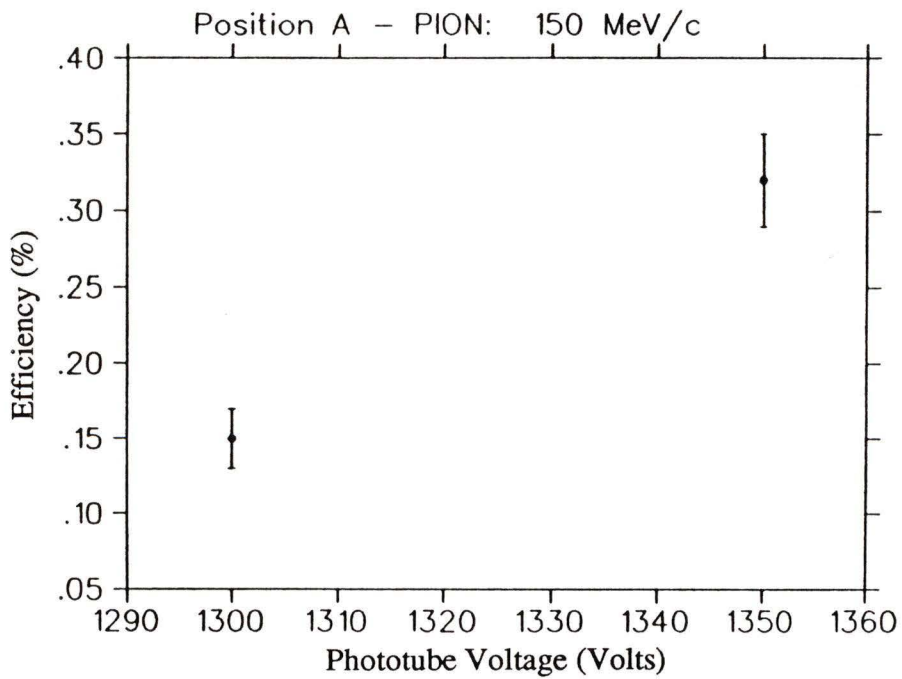
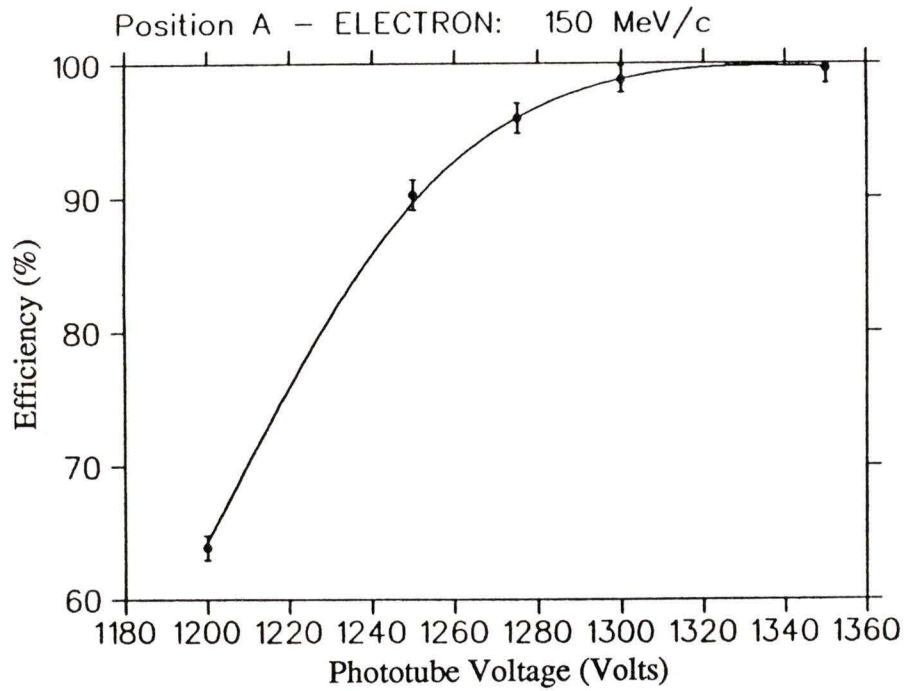


Figure 5.3: Efficiencies for position A.

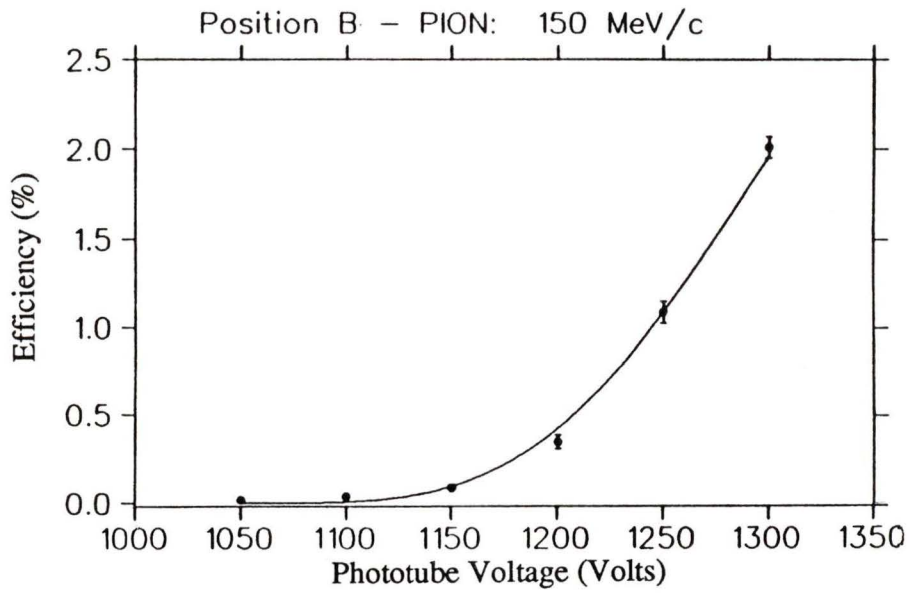
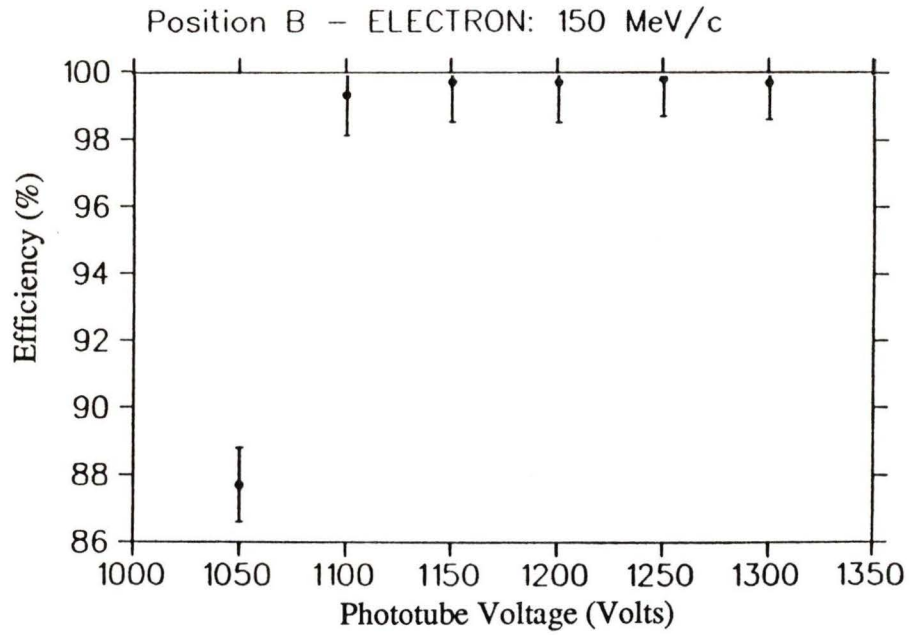


Figure 5.4: Efficiencies for position B.

Although beam time was very limited, a small sampling of efficiencies at other momenta was taken, as shown in Table 5.1. The momentum of the test beam was limited to 165 MeV/c. The large increase in efficiency to 5.3% for position B at 165 MeV/c is believed to result from the onset of Čerenkov radiation and the close proximity of the beam to the phototubes. If the pion momentum were to be increased from 165 MeV/c to 230 MeV/c, Equation (4.7) indicates that the photon count per track should increase by roughly a factor of 8. This is a point of some concern, and it may be necessary to use tracking information from the other detectors to execute a more sophisticated vetoing scheme to account for any anomalous contributions from the detector ends. Adjustment of the signal threshold levels may provide a partial solution. A compromise must be reached between maximizing the electron efficiency, which directly influences the signal-to-noise ratio, and minimizing the pion efficiency, which affects both the data acquisition rate and the effectiveness of the 2π triggering scheme.

It should be mentioned that two smaller prototypes were previously constructed with acrylic light guides (Winston cones), which were machined from solid acrylic into a funnel shape, matching the rectangular container ends to one 2" phototube (RCA 8575) on each end. The surface of the guides was covered with aluminum foil to increase the internal reflection inside the cones. Similar tests yielded nearly identical results, with electron tagging efficiencies not less than 90%, and false pion vetos not greater than 5% at 150 MeV/c. One test using only water, with no umbelliferone, yielded an efficiency of only 85% for 130 MeV/c electrons passing roughly 8 cm from one phototube, indicating that the addition of umbelliferone is a definite improvement. The acrylic light guides, however, which are very time-consuming to manufacture, were deemed unnecessary and excluded in subsequent designs. Also abandoned were various schemes to affix a reflective surface to the interior of the vessel. Noting that directionality is not required in this arrangement, no enhancement of the diffuse white inner surface of the plastic had been called

for by the efficiency results, thus eliminating complications arising from possible reactions between the umbelliferone solution and interior materials. Such a reaction was observed to blacken the surface of aluminum.

Chapter 6

Detector Fabrication Techniques

6.1 Strip-heater Forming

As the bulk of the detectors consist of water, it is desirable to minimize the possibility of leaks arising by reducing the number of joined components. Also, The final design called for container sides which were not perpendicular, and the milling and bonding of sixteen sets of such edges would have been prohibitively time consuming. A method was developed whereby the main body of a detector could be constructed by forming a sheet of white acrylic Plexiglas[®] about an internal wooden mold, as illustrated in Figure 6.1. This was then capped by an assembly used to both support the detector and couple the ends to the phototubes.

To shape the acrylic sheet, it is first made supple by resting the edge to be formed upon a hot-wire strip heater while simultaneously heating the opposite side with a heat gun. Upon reaching roughly 170⁰ C (340⁰ F), the edge becomes pliable enough to be drawn about the mold, afterwhich it is clamped in place for several minutes during cooling. Due to the large size of the sheet, the radius of curvature should be at least 2 cm for consistent results. Even at

Plexiglas[®] is a registered trademark of Rohm and Haas Co.

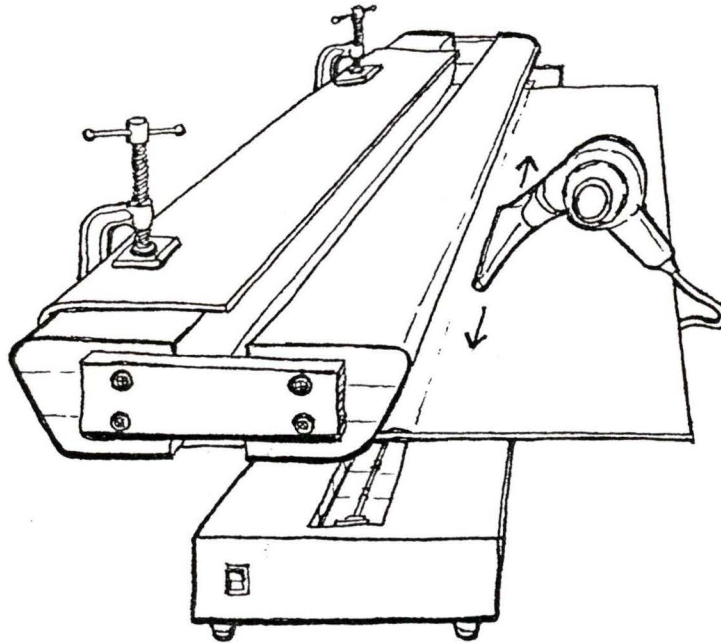


Figure 6.1: Forming a sheet about an internal mold.

this limit, irregularities in the shape will often occur at the edges, which can be removed by sculpting with a heat gun.

After inspecting the completed form with a template matching the outside tolerance of the design, the overlap along the length of the detector is cut away using a circular saw, leaving a gap of a few millimeters which, after reforming the last edge so the top is level, is sealed with a bonded acrylic strip. The result is an exceptionally strong midsection which may be rapidly reproduced.

6.2 Bonding Techniques

With the form still firmly clamped about the mold, a catalyzed acrylic resin, known as Acrafix[®], is used to bond the top strip to the main body. It is important that not too much stress is restrained by the clamps, as it may be sufficient to fracture the acrylic afterwards. A cardboard trough is inserted between the two main spars of the mold to ensure resin does not drip to the bottom surface nor contact wood at any point. After several hours of setting, the mold may be dislodged by removing the wooden braces separating the two spars, then drawing them together and out, as in Figure 6.2, simultaneously scissoring any dripping glue that has hardened. The mold is later reset by using templates which match the internal profile of the vessel.

After the completed form is cut to roughly the required length, holes are drilled and tapped in opposite corners of the inner face for fluid caps. Any glue or marks from the mold on the interior surface are then polished out with various grades of acrylic abrasives.

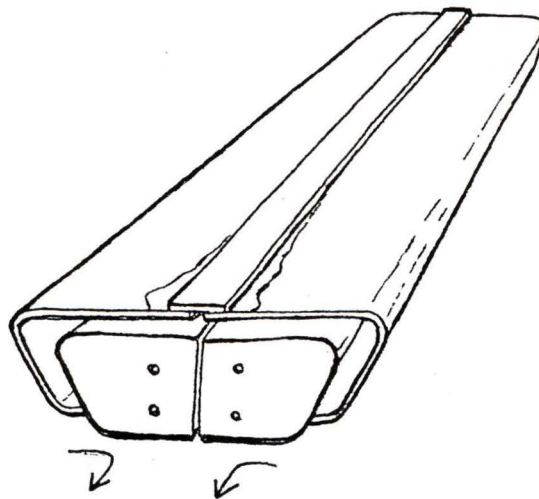


Figure 6.2: Removing the mold from the form.

When two pieces of acrylic can be brought together such that there is no visible gap between them, a more desirable method of joining them, known as solvent bonding, may be used. In this method, the two pieces are cleaned with alcohol and placed as close as possible without being clamped under pressure. A hypodermic syringe is then used to rapidly apply a solvent for the acrylic, dichloromethane (methylene dichloride), along the length of the exposed periphery of the area to be bonded. The solvent is then drawn between the two pieces by capillary action, forming a joint which is essentially the same as a continuous section.

This method is particularly useful in joining the two clear acrylic windows to the black endplate, depicted as (A) in Figure 6.3. The disks may be lathed in groups and melded in place neatly with no possibility of leaks arising. The precision milled bottom support block is also solvent bonded to the endplate, with the aid of brass pins to align the lower three of the six mounting holes.

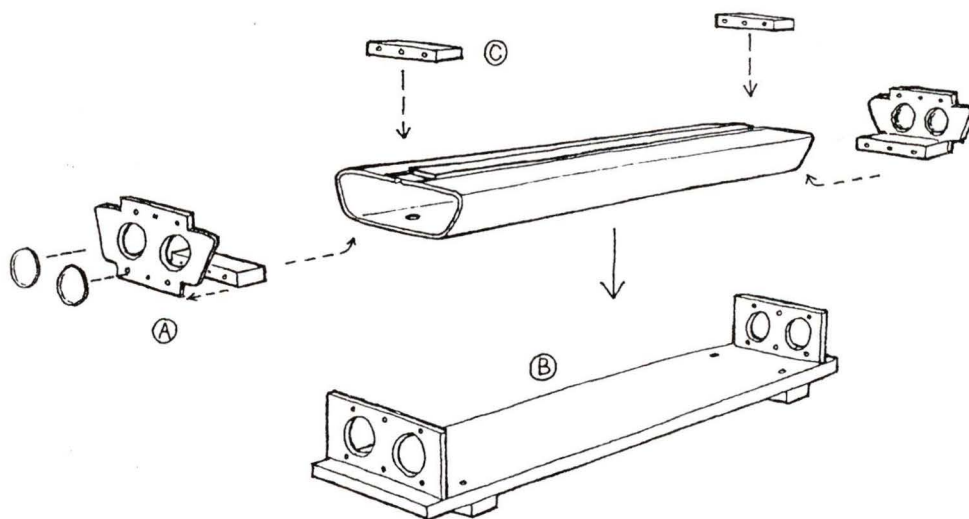


Figure 6.3: Final assembly of the subcomponents.

The endplates are fabricated from stock sheet, which tends to vary in thickness by roughly 10%, requiring that the midsection then be milled to fit to a specific pair of endplates. The top strip is then machined away where the top support block is to rest. Liberal amounts of Acrafix are then used to bond the endplate subassemblies to the midsection, with the exception of the area directly above the windows to avoid glue running down their inside surfaces. Before the resin begins to set, the detector is placed in a precision aluminum jig (B), which has been aligned to emulate the final support structure. Resin is applied to affix the top support block, with all parts then held in place by striking brass pins into the twelve support holes. Solvent bonding is not appropriate in these latter stages due to irregularities arising in the molding of the midsection. Variations may be compensated for by shimming or sanding the support blocks prior to gluing.

After 24 hours, the vessel may be removed from the jig by hammering out the pins and cracking any overflowed resin, which does not adhere firmly to brass or aluminum, particularly if a thin layer of machine oil is applied to these surfaces prior to gluing. The detector is then wrapped with two layers of 0.25 mm thick black vinyl sheet, with the exception of the end faces, which are subsequently sealed from ambient light when the entire ring of detectors is assembled at the experiment site. The design of the endplates, with the concave areas at the corners where the main body attaches, made it difficult to achieve light isolation using tape. Also, the bonding resins used tended to act as light guides between the joints, so additional tape was required at these edges.

The original valve inserts, as used in the prototype, were later replaced during installation by thin black threaded polyethylene plugs to allow more space inside the detector ring.

6.3 Phototube Mounting

As the final assembly step, a two part silicone rubber compound (General Electric RTV615), mixed by the standard component ratio, is poured into each basin formed by a window in the thicker endplates. Each window is 6 mm in depth, bonded such that the inner surface is flush with that of the interior of the detector endplate. The depth of the overlaying silicone is roughly 4 mm. After setting, this provides a pliable optical contact surface for the phototubes. The silicone must be covered prior to mounting in order to protect the surface from contaminants.

The detectors themselves are each held in place by twelve stainless steel pins, six on each side passing through a large 20 mm thick aluminum endplate encompassing all sixteen detectors, then into the mounting holes of each vessel. The phototubes are then introduced through appropriate holes cut in the main plate. Due to earthquake regulations in Japan, there is a gap of 0.5 mm between the detector endplates and the main mounting plate, with a spring assembly on each of the smaller center pins to dampen vibrations to the vessels. This is illustrated in Figure 6.4¹, which also shows the support plates used to hold the magnetic shields, which in turn contain the phototubes. These shields, manufactured by Hamamatsu Photonics Co., are constructed from a mu-metal alloy which serves to protect the sensitive workings of the phototubes from ambient magnetic fields. These structures may also be seen in Figure 3.2.

¹Figures 6.4 to 6.8 were extracted from blueprints provided by the Tokyo KPX group.

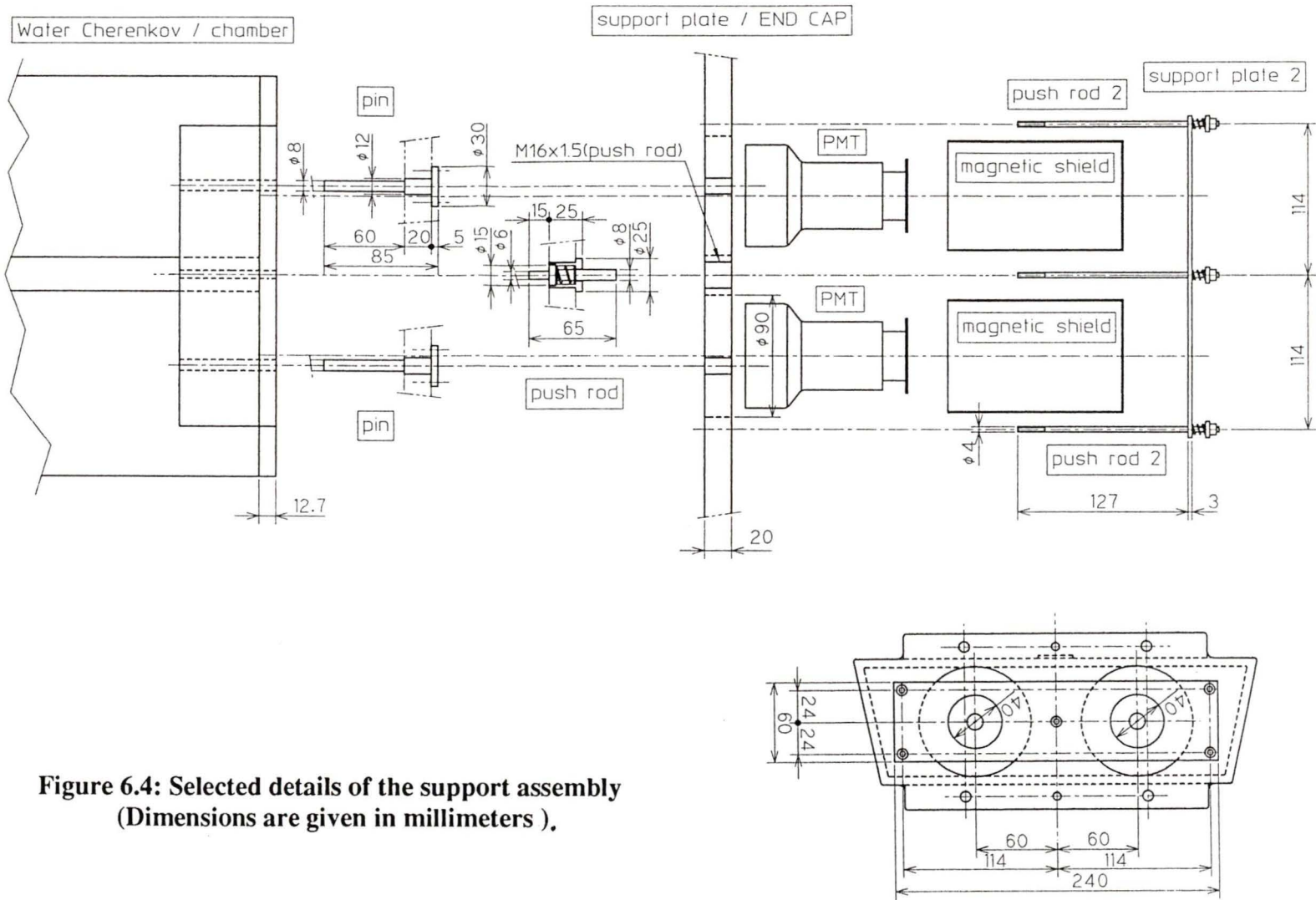


Figure 6.4: Selected details of the support assembly (Dimensions are given in millimeters).

6.4 Final Design Dimensions

Dimensions for the final design are presented in Figures 6.5 to 6.7, which may be useful in the construction of similar acrylic containers. Only one end is shown as the opposite one is identical. The overall length of a detector, measured from the exterior of the endplates, is $1179 \text{ mm} \pm 0.2 \text{ mm}$. This tolerance ensures that negligible stress is imposed on the joints in the event of thermal expansion or vibration, as might occur if one corner of a detector endplate were not flush with the support plate.

The detectors fit together in the final array to within roughly 3mm between the sides of adjacent vessels. This is to allow for light shielding around the sides, which is not shown in Figure 6.5. The main endcap support plate was assembled from two crescent shaped plates of aluminum, joined by a matching plate at the midsection, details of which are shown in Figure 6.8.

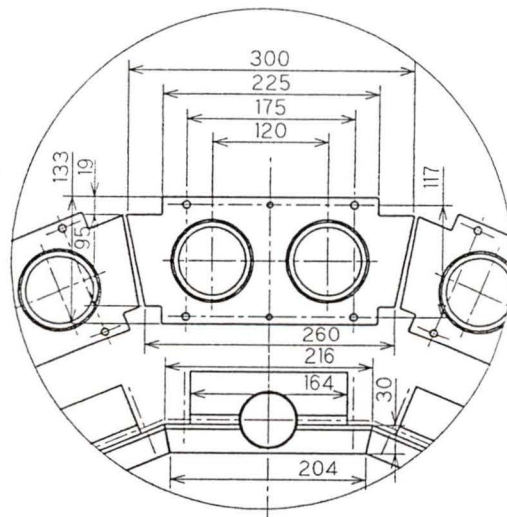


Figure 6.5: Diagram showing the proximity of a Čerenkov counter to neighboring ones.

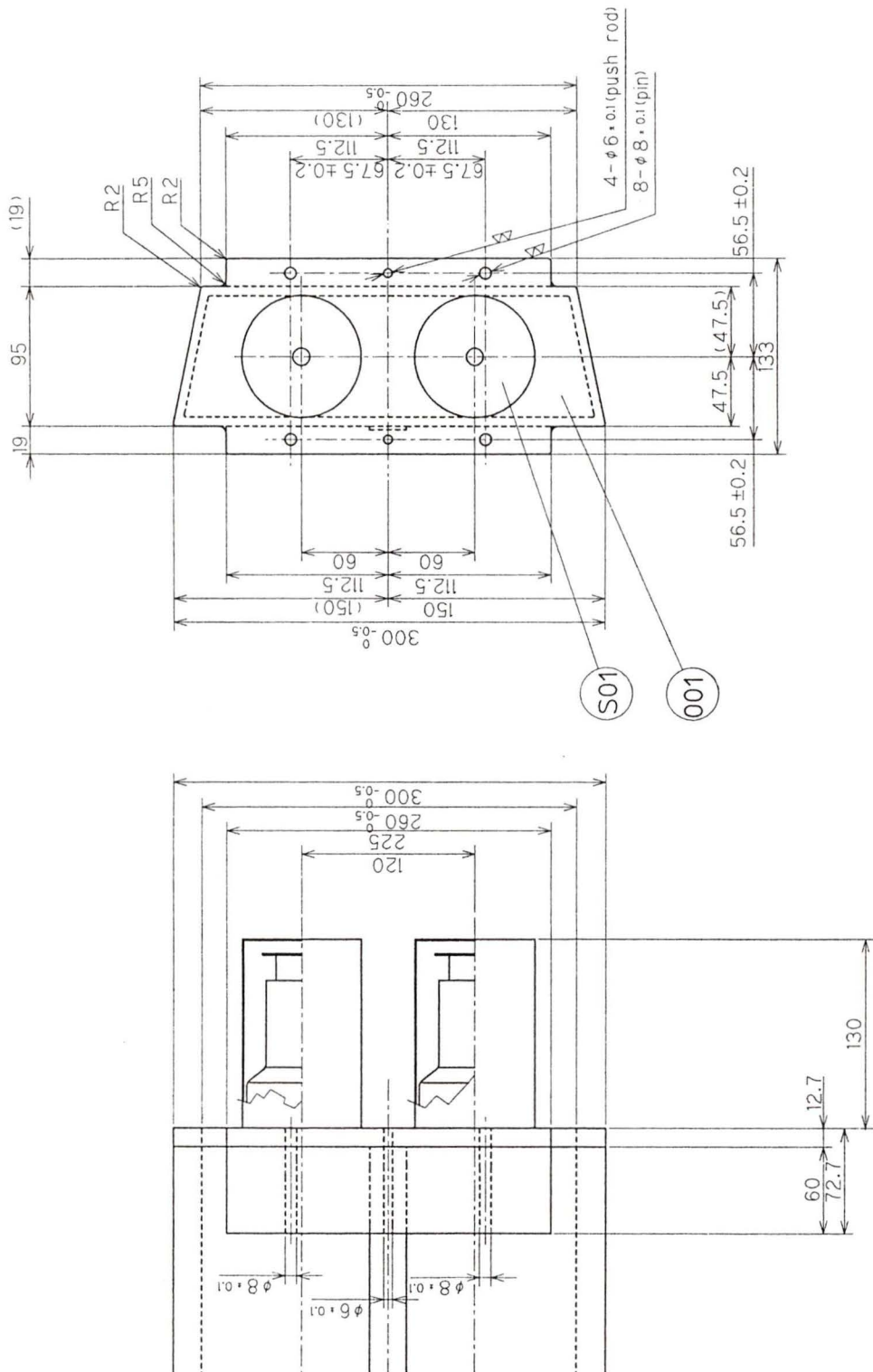


Figure 6.6: Top and front view details of the final design.

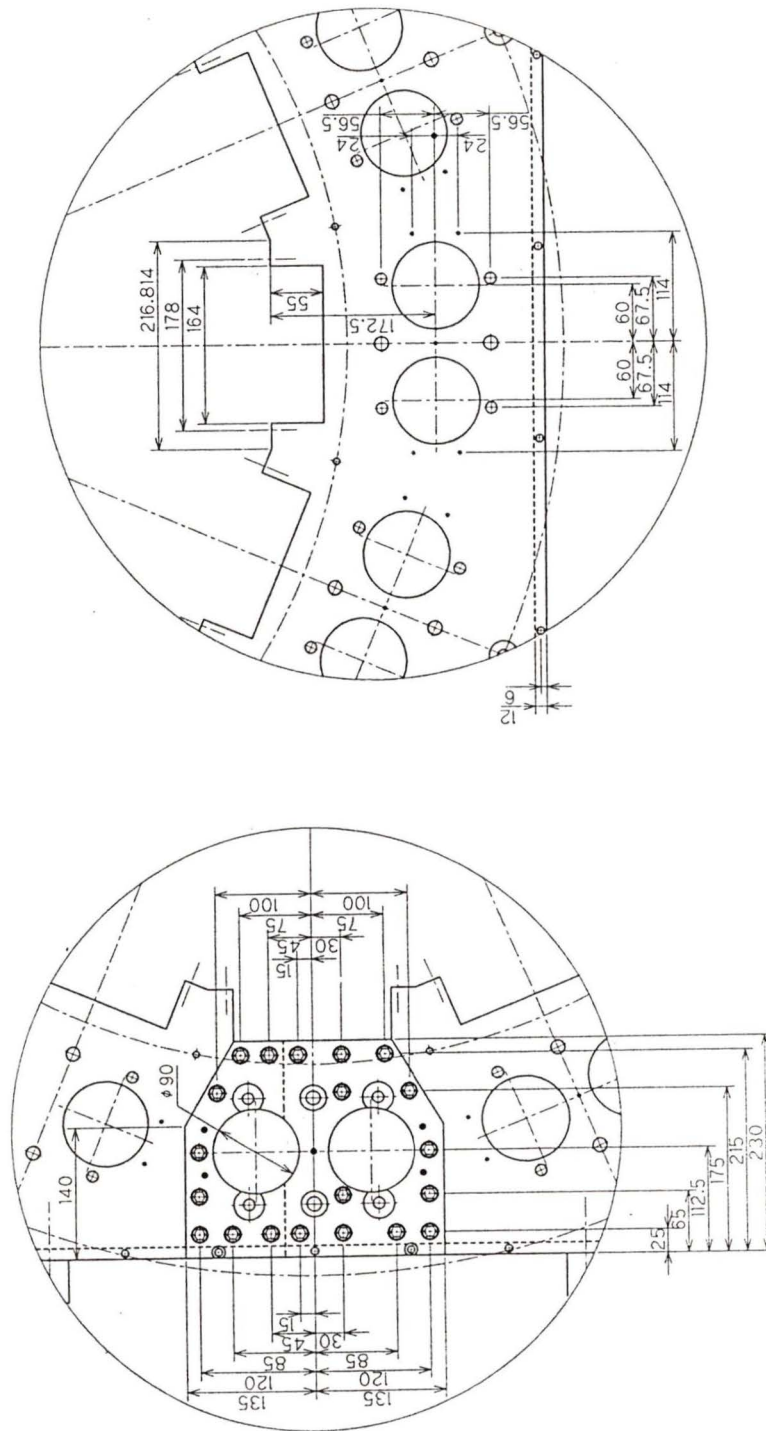


Figure 6.8: Selected details of portions of the main end cap support plate.

Chapter 7

Testing of the Completed Array

7.1 Cosmic Ray Testing

After final assembly, the Čerenkov detectors are arranged in a cylinder about the beam axis at a radius of 0.7 m (see Figure 3.3). Therefore direct use of the beam to test the discrimination efficiency is not geometrically possible. However, one may still monitor their performance by detecting cosmic ray particles. At sea-level, this flux is mainly composed of high energy muons and electrons, both of which should trigger the veto array. Cosmic rays may be identified by the T2 scintillator arrays; then the Čerenkov counters are examined to determine counter efficiencies over the entire ring and for sections of the individual Čerenkov containers.

The analog outputs from four phototubes per Čerenkov detector are mixed, and then routed through an integrating amplifier (time constant = 0.1 ms, gain $\approx 5x$) to filter out most of the electrical noise from the phototubes. The signal is then converted to digital data, with the intensity of the signal designated ADC (analog to digital conversion), and the time interval between an event which triggers data acquisition to that of the signal pulse designated TDC (time to digital conversion).

Figures 7.1 to 7.4 show the ADC profiles for each Čerenkov detector from a data set of roughly 2.2×10^6 events, where data acquisition is triggered by the detection of at least one signal from the T2 array, which is more sensitive than the Čerenkov array. Here, the number of counts for each ADC value (ADC in arbitrary units) is presented in a logarithmic histogram. Below an ADC value of roughly 500 there exists a large peak due to low level noise from background photons in the detectors, which is filtered out in data analysis. A qualitative comparison of such plots among the detectors was used to set the phototube voltages, supplying voltage to only one phototube per detector in turn, in an attempt to standardize the sensitivity of the array.

Figures 7.5 to 7.8 display the TDC data from the Čerenkov (WC) detectors. The histogram abscissa represents the time at which a pulse was received from the WC detector, after a small cable delay, relative to the start of a data event triggered by any T2. Therefore, the presence of the peaks indicates that the WC signals are well correlated to the T2 triggers, as one would expect a flat random histogram if the WC signals were not related to the same events which triggered the T2 array.

The T2 detectors provide two signals, one from each phototube at opposite ends of a detector. If a pulse from the same cosmic ray hit is received at both ends, one may then use the difference in the TDC values from either side to measure the the position of a hit along the length of the scintillator. Histograms of this time difference, shown in Figures 7.9 to 7.12, determine the limits corresponding to the scintillator ends. This information may be used to infer the position of a track along the length of the Čerenkov detector directly alongside each T2, provided one examines only cases where the cosmic ray penetrates directly through the ring, intercepting the beam axis and triggering the opposite T2. The position resolution of this technique is limited to roughly 1 cm due to the lack of transverse position information.

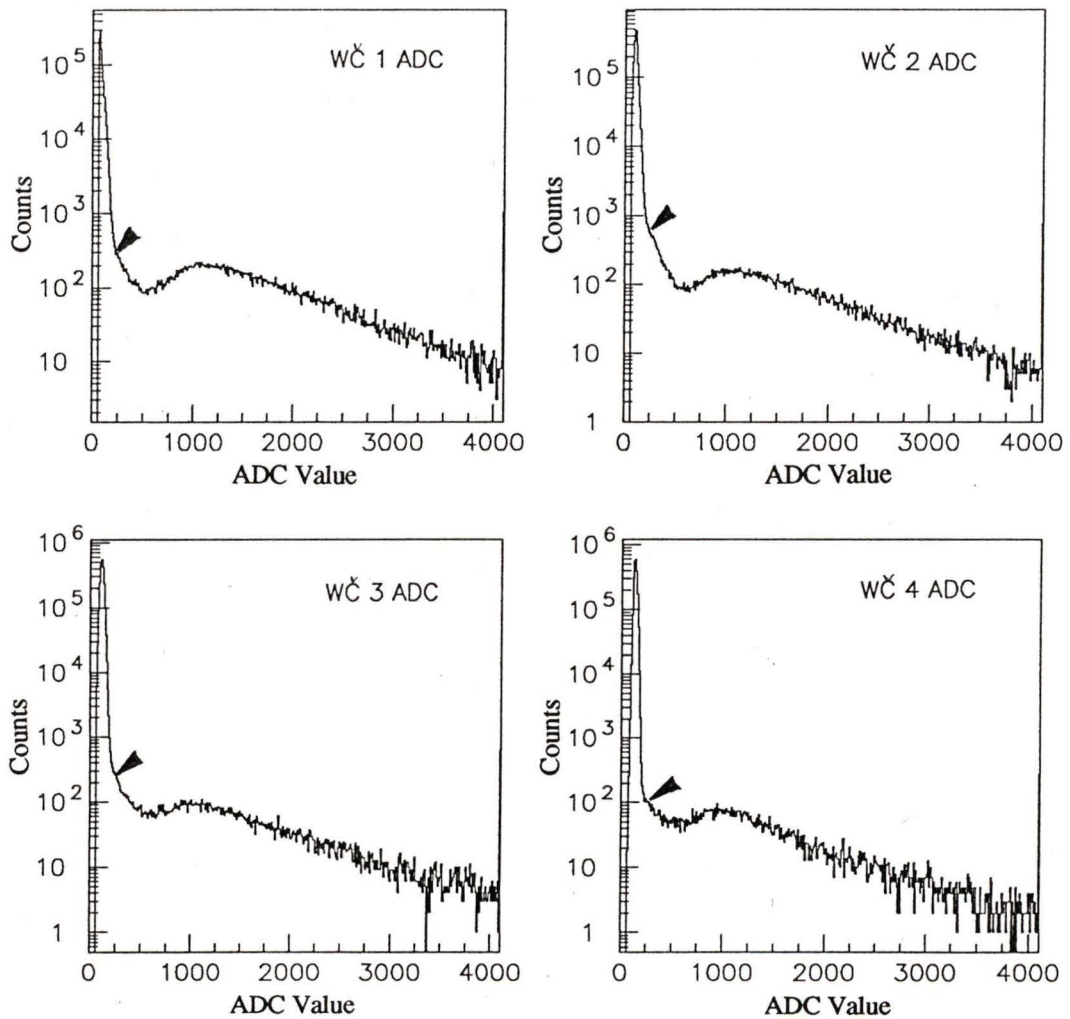


Figure 7.1: Histograms of Čerenkov ADC values (Detectors 1 to 4). Markers indicate the position of ADC cutoffs used in the program listed in the Appendix.

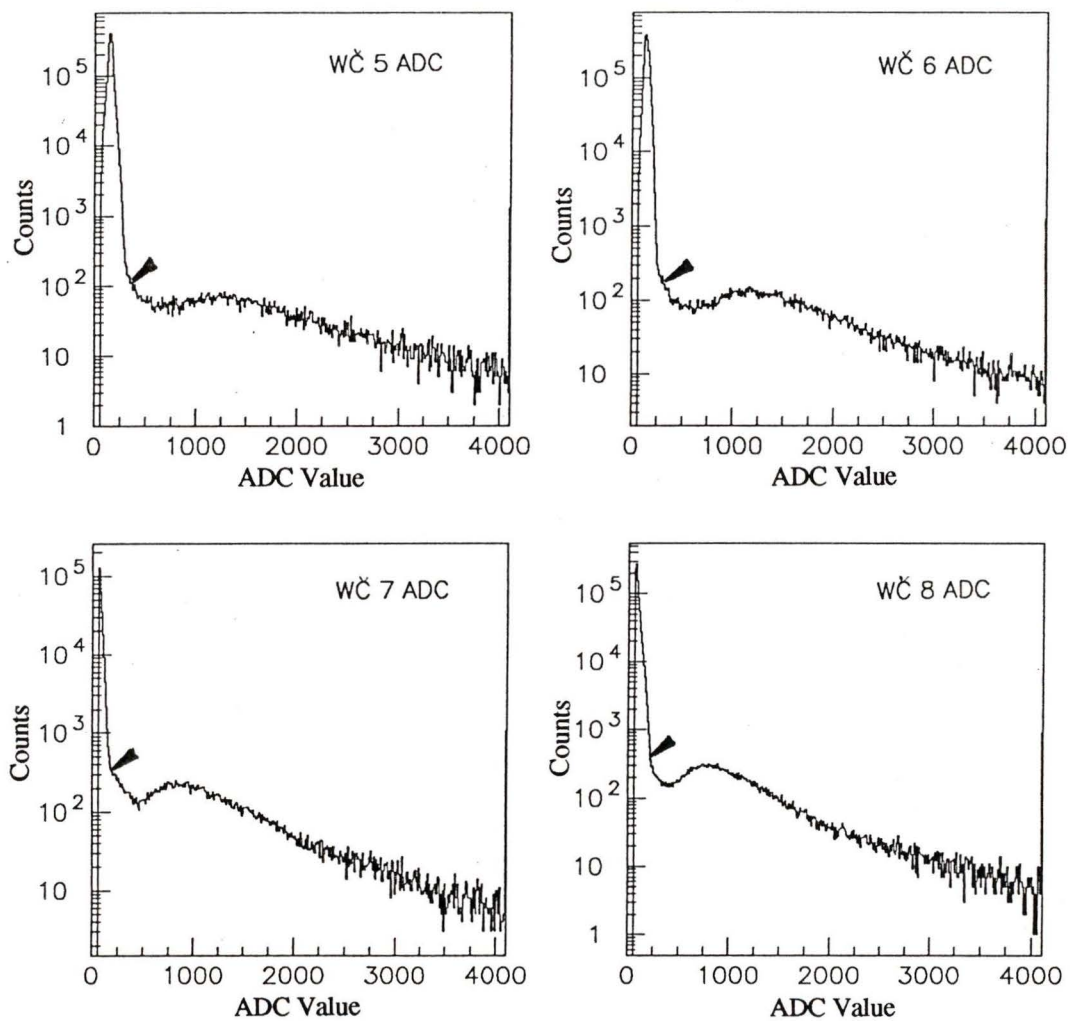


Figure 7.2: Histograms of Čerenkov ADC values (Detectors 5 to 8).

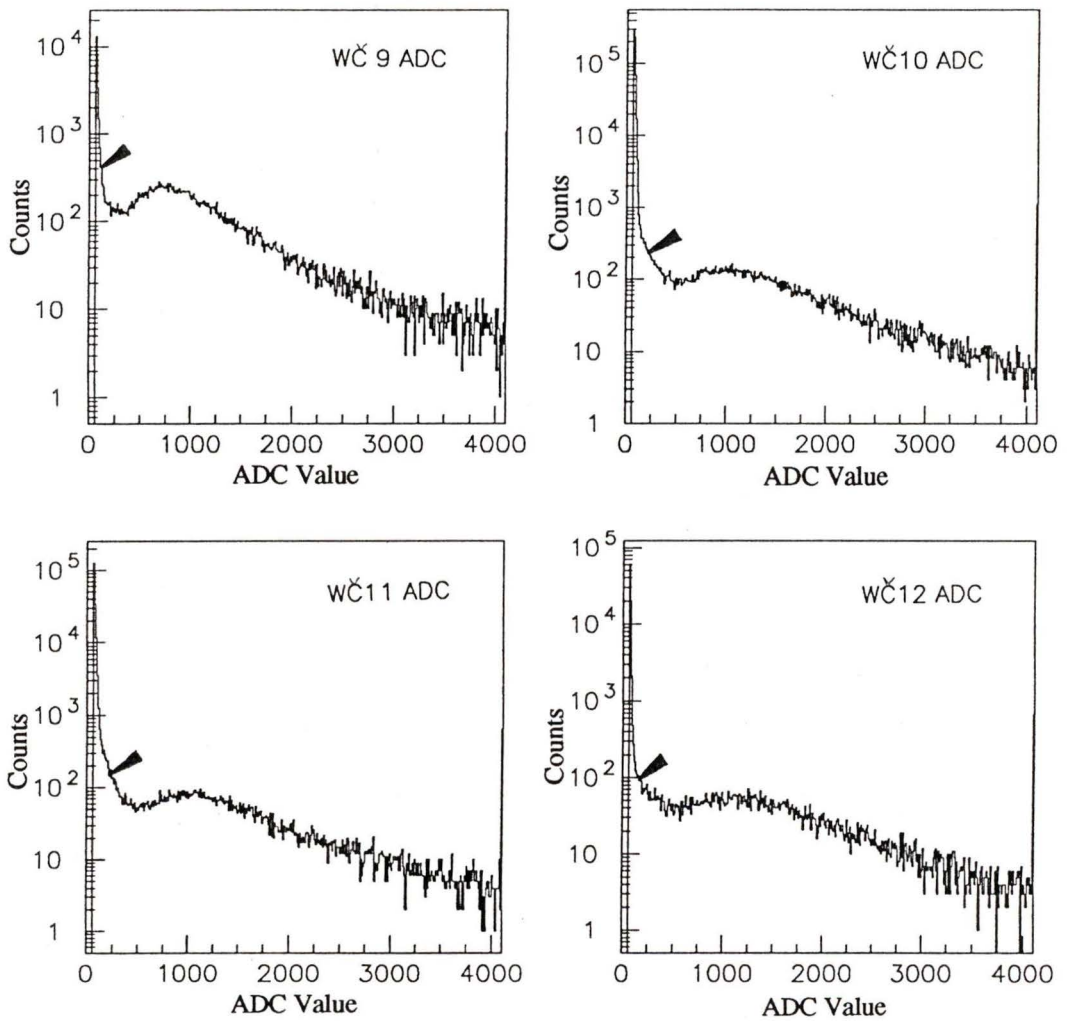


Figure 7.3: Histograms of Čerenkov ADC values (Detectors 9 to 12).

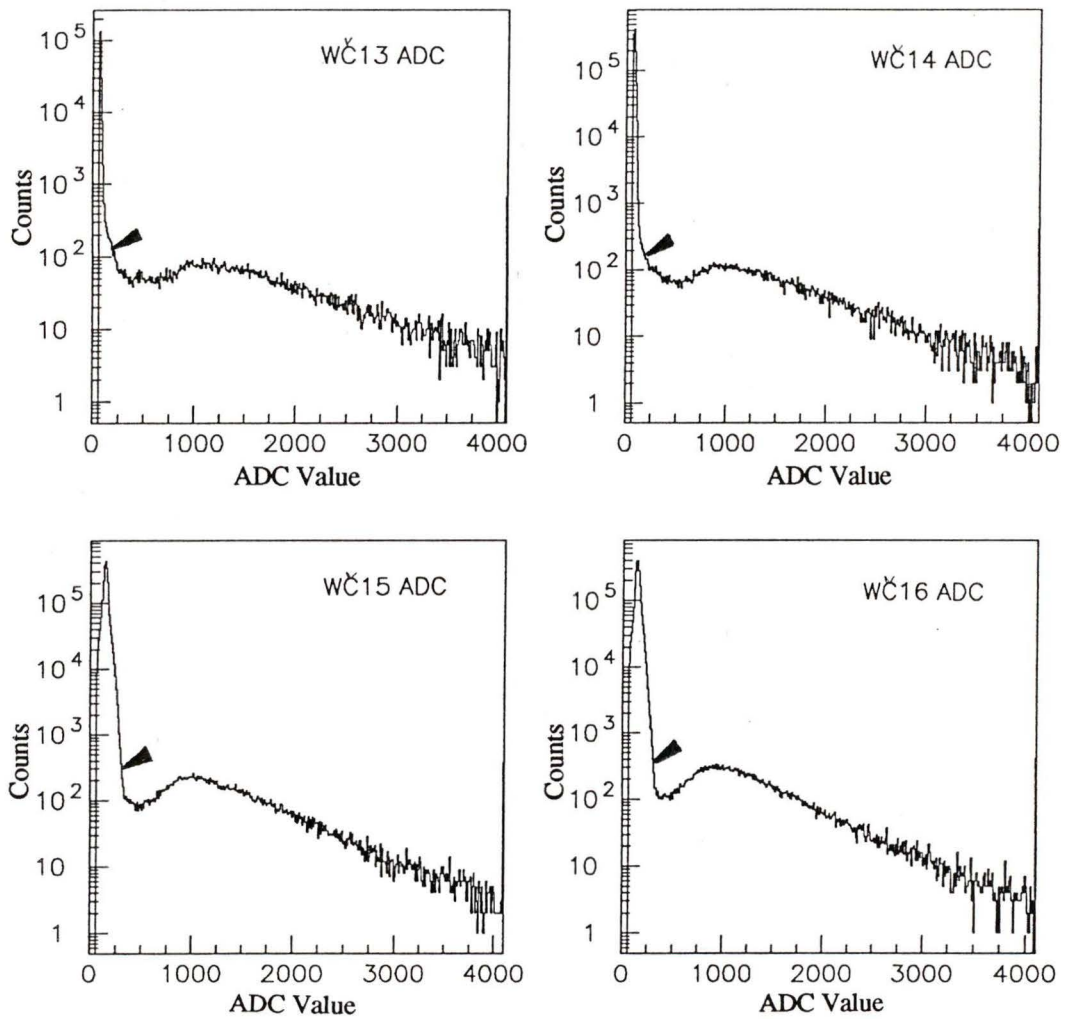


Figure 7.4: Histograms of Čerenkov ADC values
(Detectors 13 to 16).

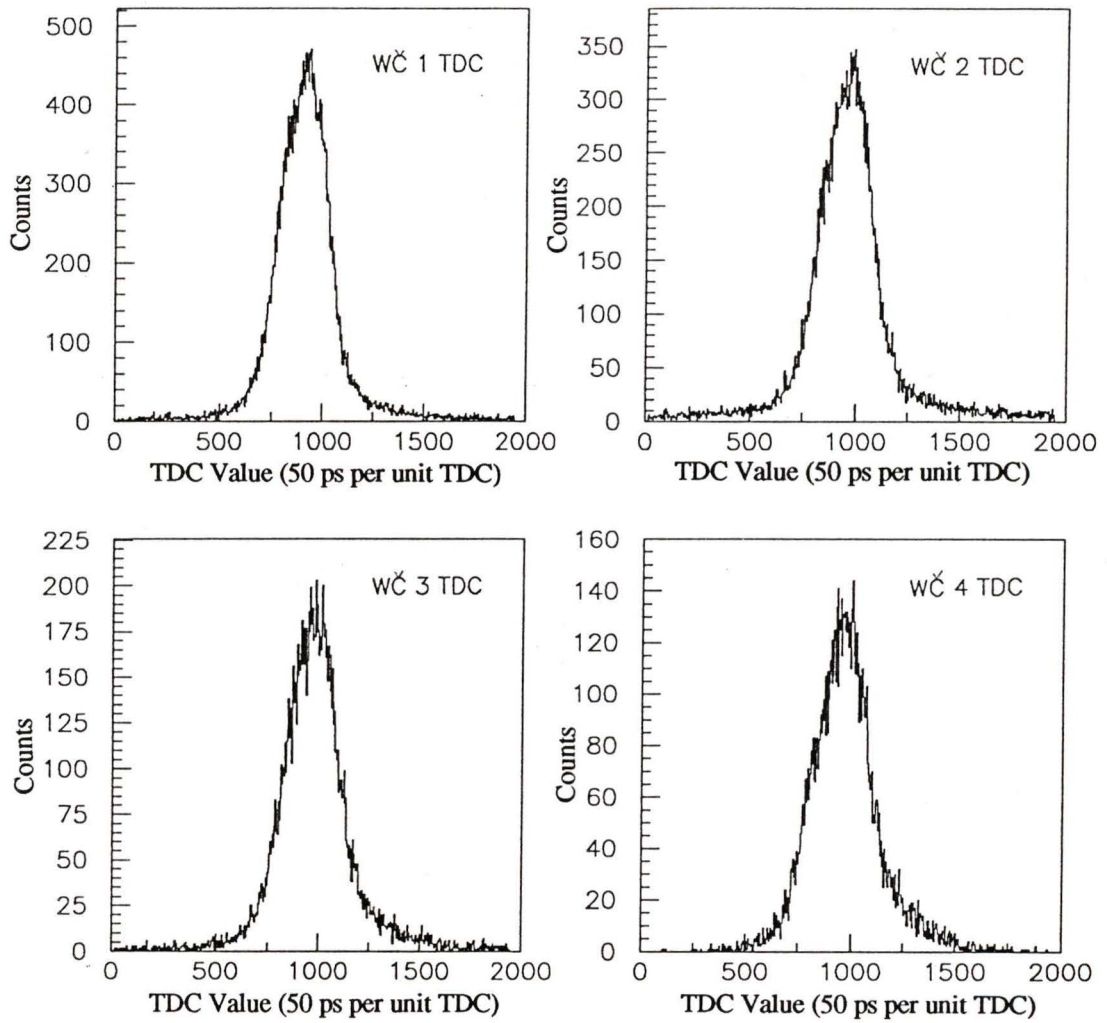


Figure 7.5: Histograms of Čerenkov TDC values (Detectors 1 to 4).

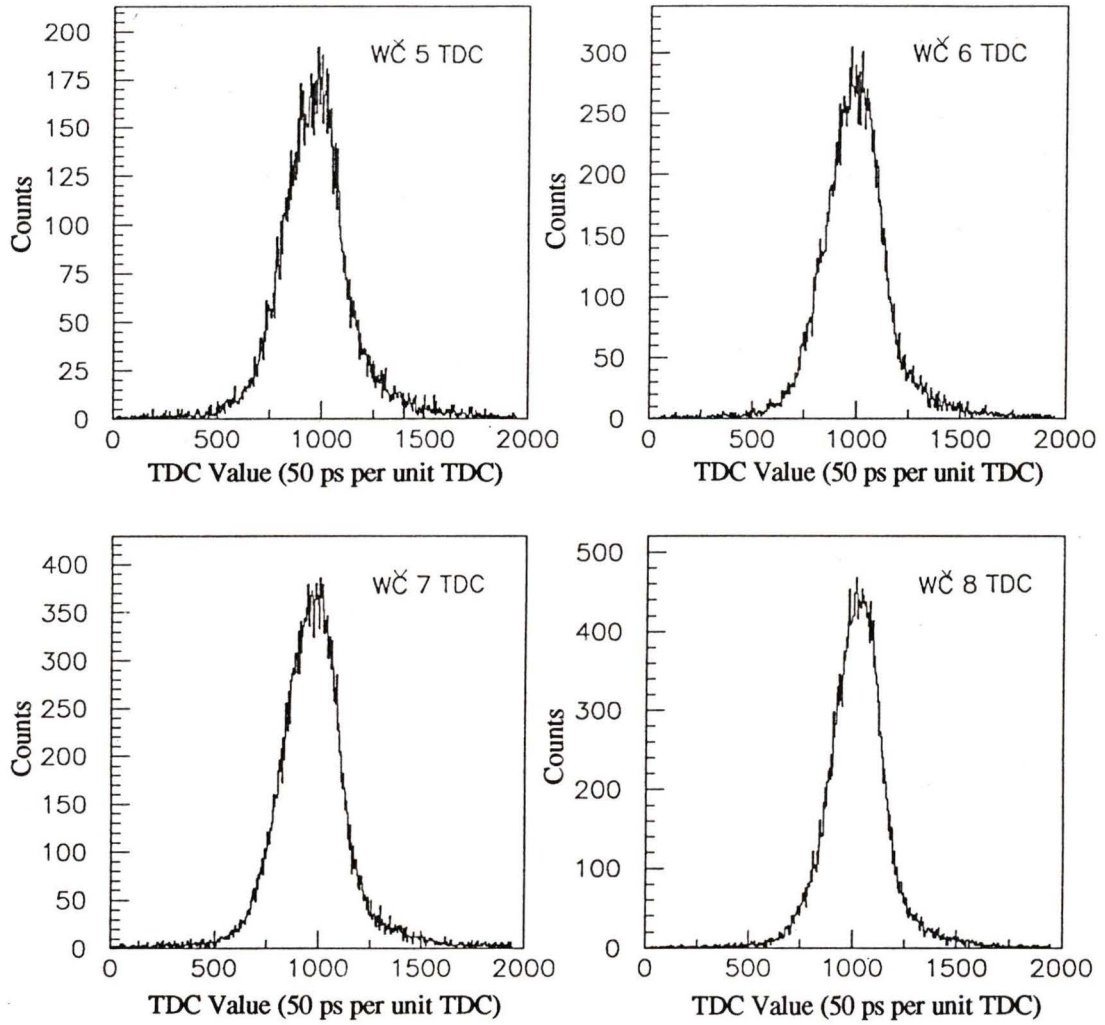


Figure 7.6: Histograms of Čerenkov TDC values (Detectors 5 to 8).

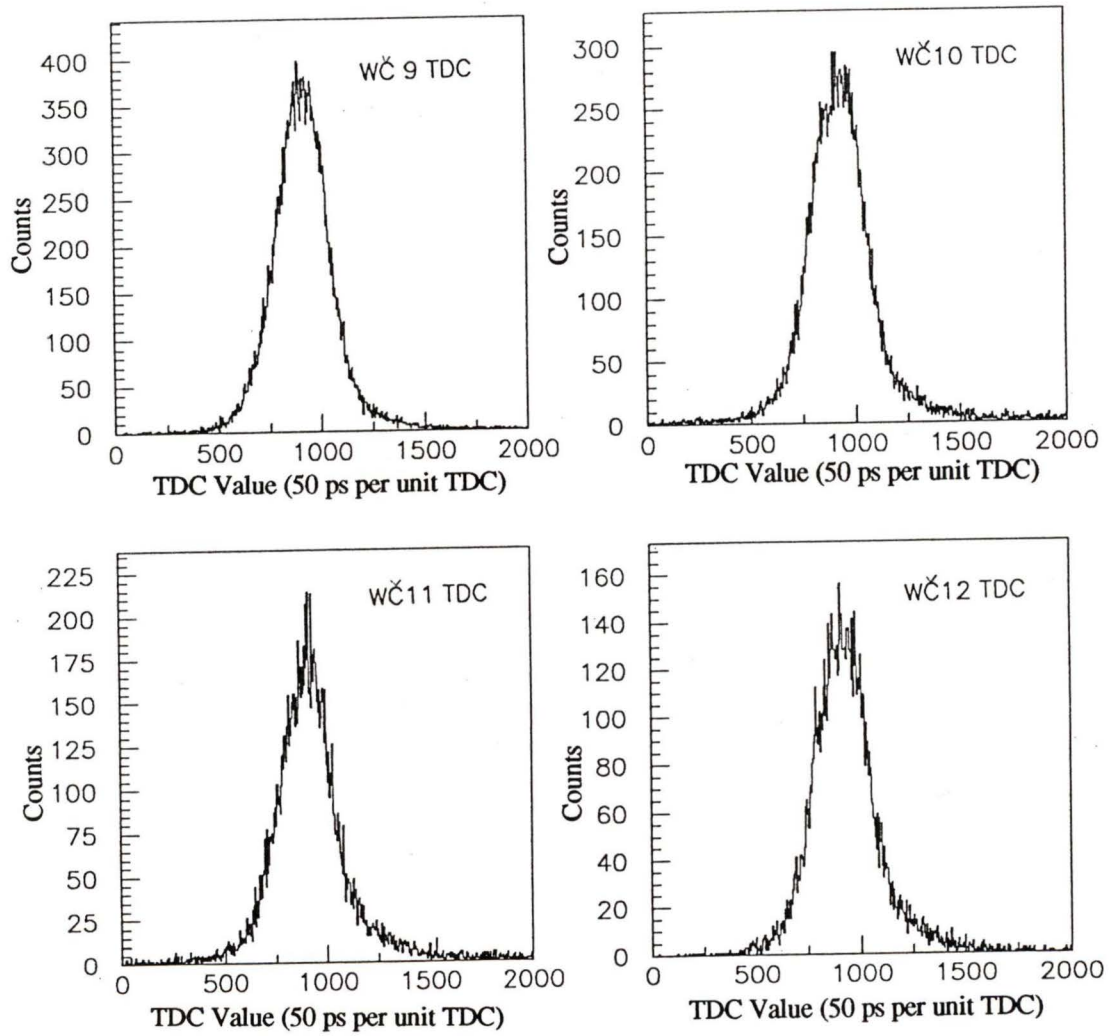


Figure 7.7: Histograms of Cerenkov TDC values
(Detectors 9 to 12).

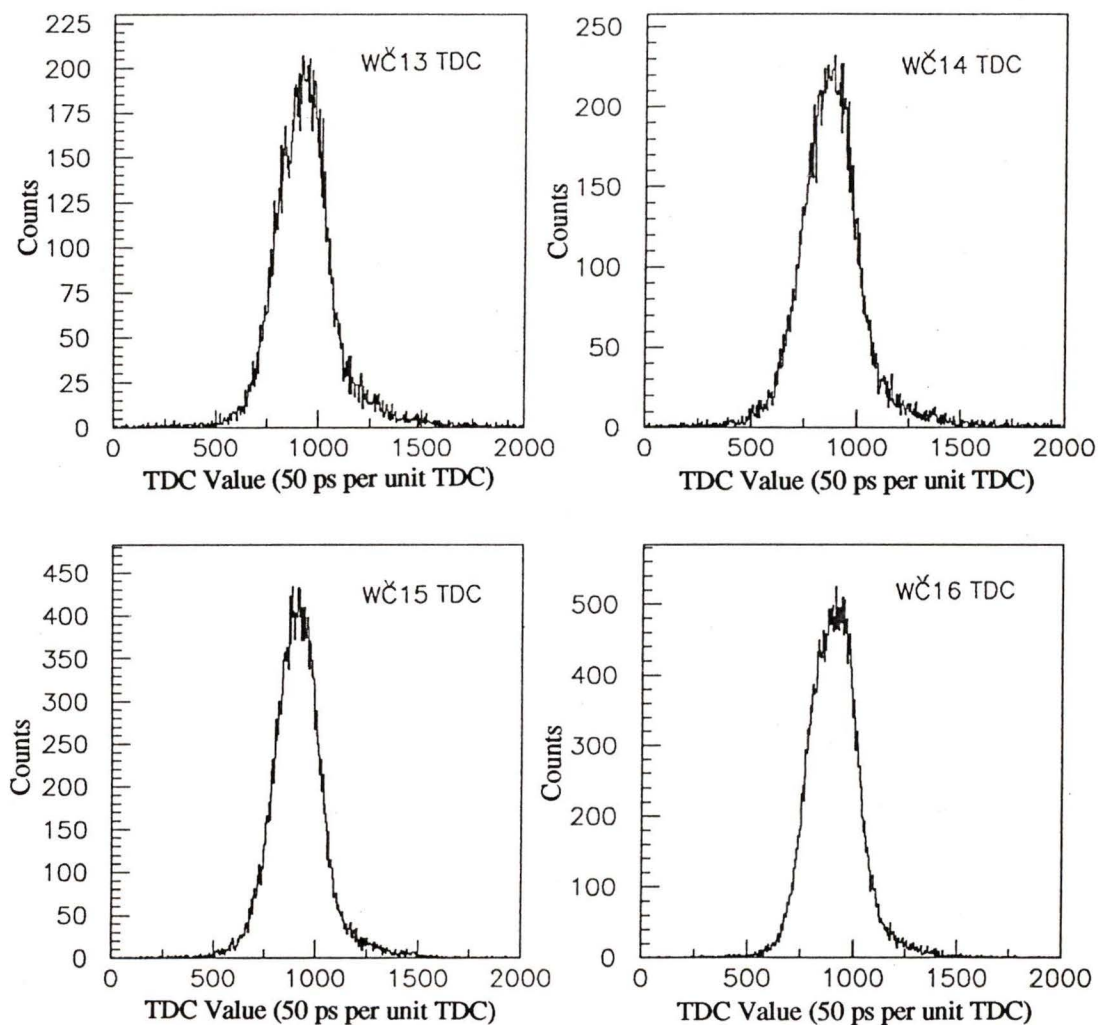
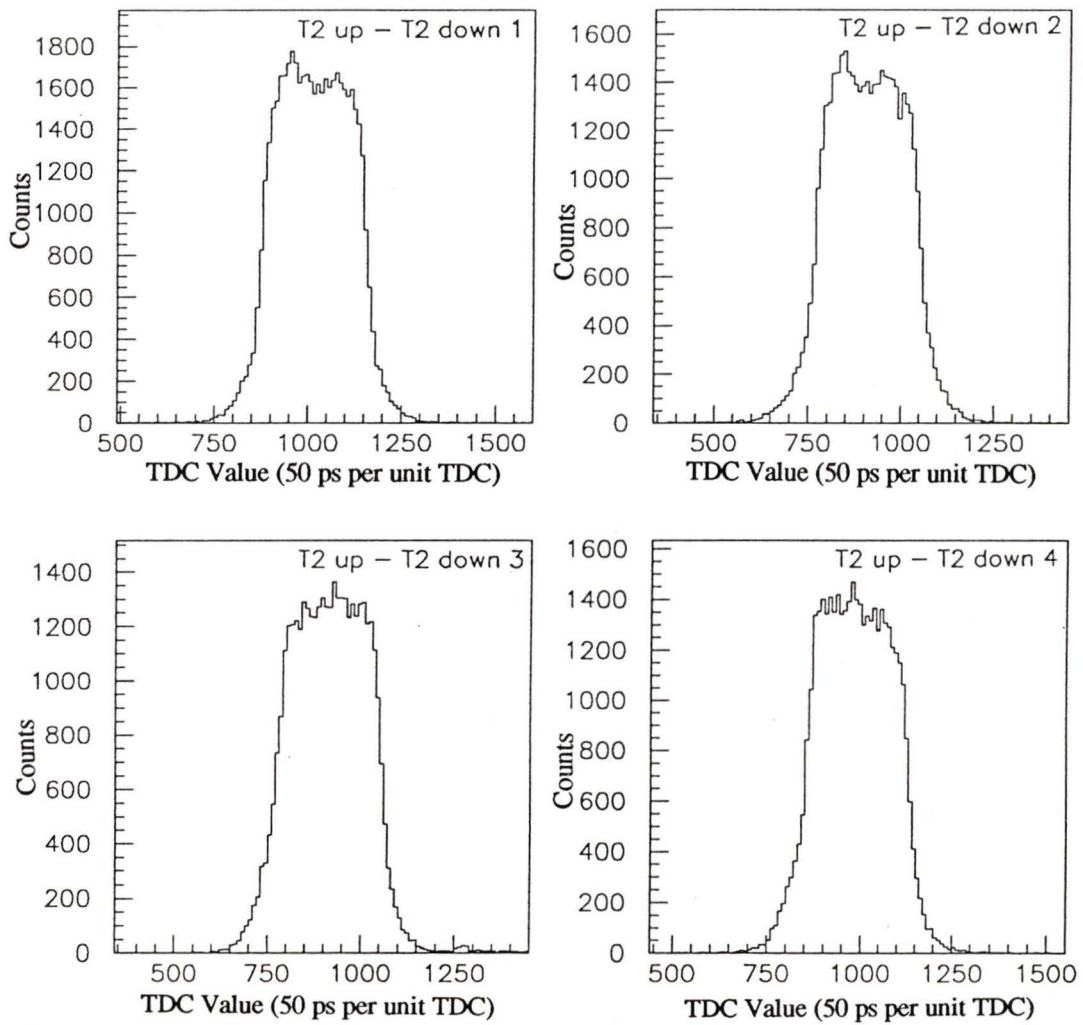


Figure 7.8: Histograms of Cerenkov TDC values
(Detectors 13 to 16).



**Figure 7.9: T2 TDC profile histograms
(Detectors 1 to 4).**

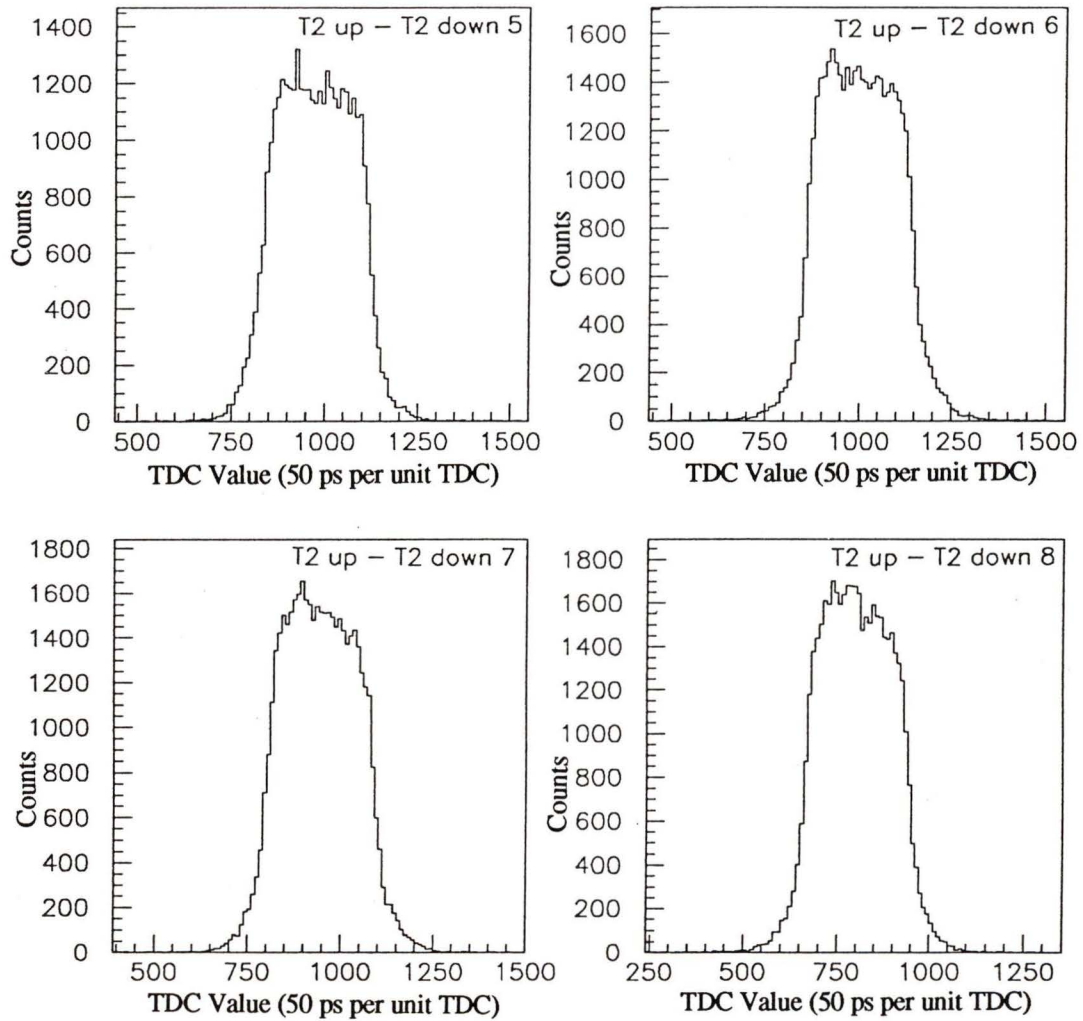


Figure 7.10: T2 TDC profile histograms
(Detectors 5 to 8).

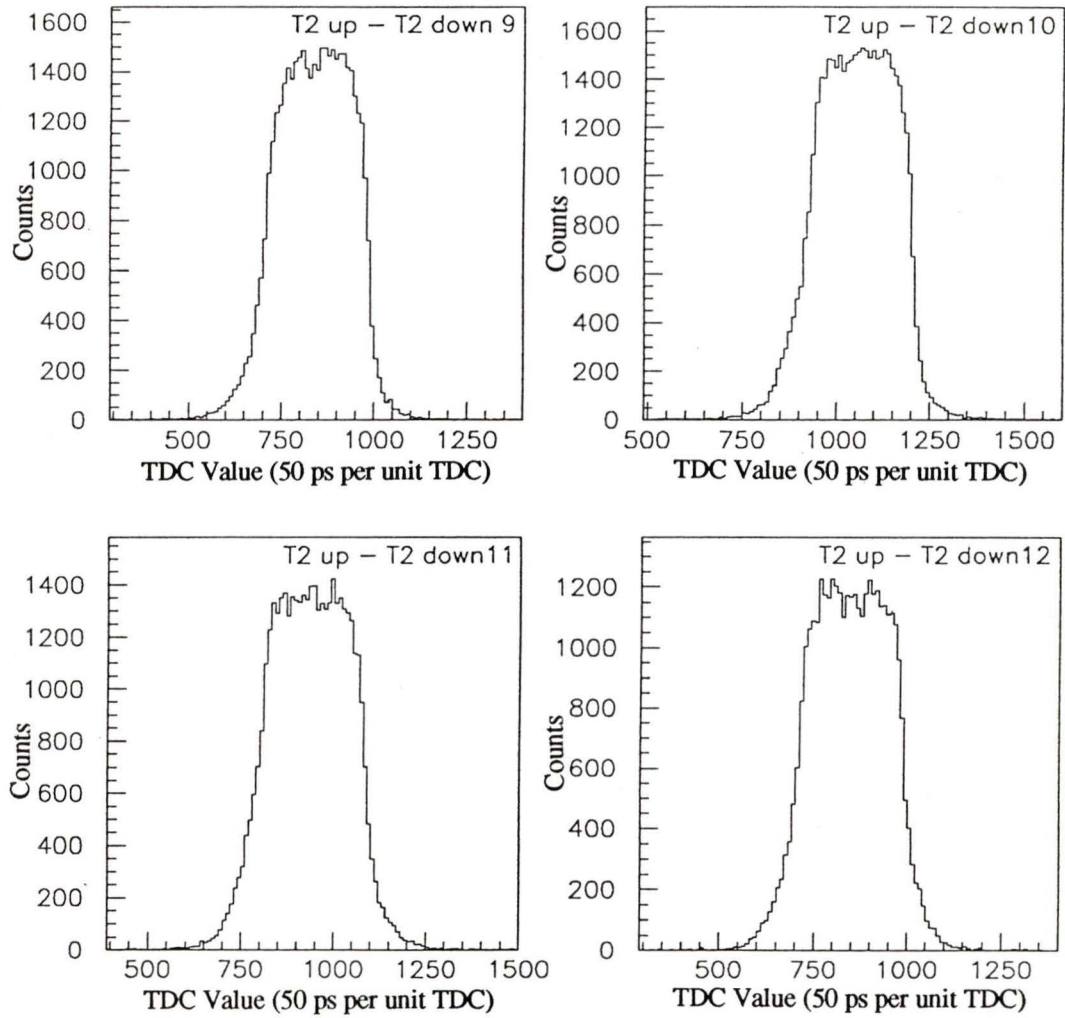


Figure 7.11: T2 TDC profile histograms
(Detectors 9 to 12).

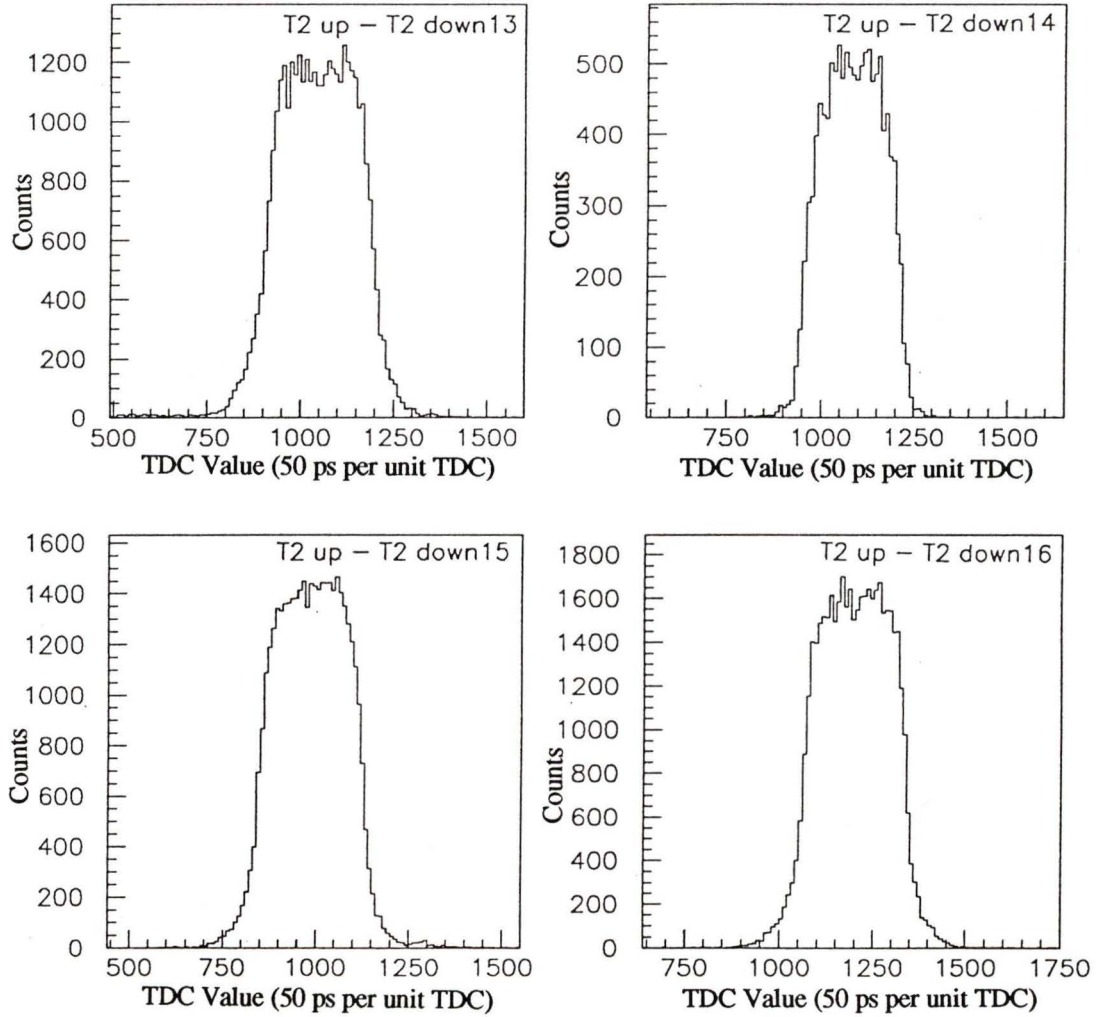


Figure 7.12: T2 TDC profile histograms (Detectors 13 to 16).

The total number of counts recorded by each detector is displayed in two ways. A "hitpattern" may be formed by plotting the total number of counts each individual detector produces in a data run, versus the detector's position number. The detectors are numbered sequentially, ending in number 16 directly at the top of the array. A "multiplicity" plot may also be made showing the number of detectors which were triggered by a single event. Multiplicity plots for the WC and T2 arrays are shown in Figure 7.13. They indicate that the events of TDC multiplicity=1 should be filtered out in the data analysis if cosmic rays which pierce the entire array are to be used to determine the WC efficiencies. There is some control over the WC TDC single multiplicity rates to be filtered by adjusting the WC ADC cutoff levels used in the analysis program. The general criterion used was to lower the cutoff values to accept more events, but only to the point where the single WC TDC multiplicity rate was comparable to that of the double multiplicity rate.

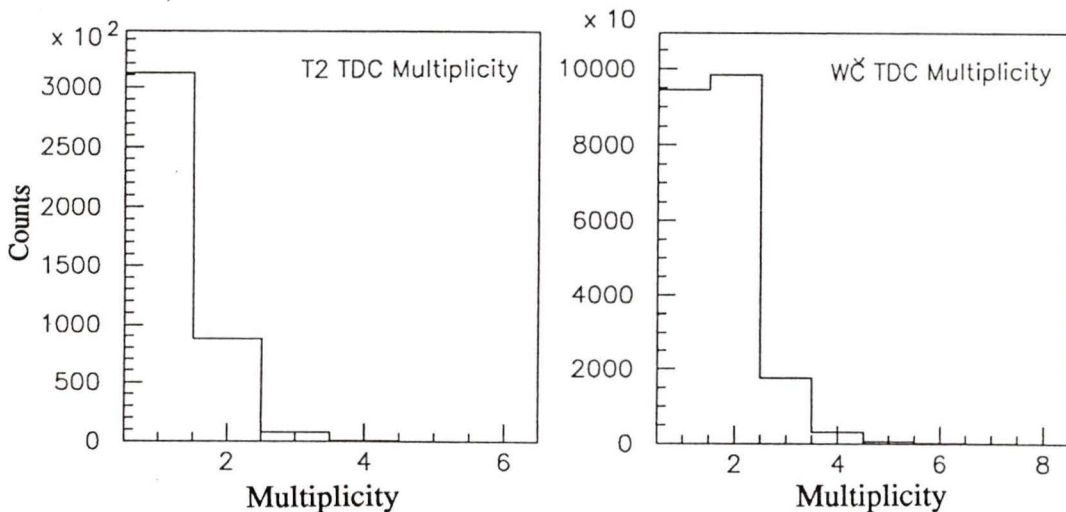


Figure 7.13: Multiplicity plots for the T2 and WC arrays.

The hitpatterns for both WC and T2 data are shown in Figure 7.14. The only restrictions here are that a signal must be received from both ends of a T2 to register, and the WC ADC value must be above the set threshold. Evidence of cosmic rays is apparent in the first two plots, as the detectors near the top and bottom exhibit a higher count rate due to their larger profile with respect to the predominantly vertical cosmic ray tracks. The low count rate in T2 TDC #14 indicates a problem (see Figure 7.14), but this does not seriously hinder the efficiency calculations to follow. It is known that T2 #14 has the shortest cable length from the detector, and hence a hardware triggering problem is suspected.

The last plot of Figure 7.14 demonstrates the effectiveness of the cosmic filter used in the data analysis. The only requirement here is that a T2 triggers at both ends, along with the T2 directly opposite in the ring, and that T2 multiplicity=2. The marked absence of such events in channel #4, corresponding to horizontal tracks, is clear evidence that the triggers are from piercing cosmic rays.

7.2 Efficiency Results

The program listed in the Appendix was used to calculate the veto efficiency for each WC counter according to its ability to detect the signals identified as piercing cosmic rays by the T2 data. In each cosmic ray event, if one of the adjacent WC detectors triggers, then the WC directly opposite is also expected to register, as illustrated in Figure 7.15. The fractional number of times this actually occurs then defines the efficiency of a Čerenkov counter. The results of this method are displayed in Figure 7.16, which shows the number of times each WC should have triggered under $(WC * T2)$, followed by the number of times it did under the criteria expressed logically in Equation (7.1). Here, (i) denotes position number i around the array, and $(i+8)$ denotes the position directly opposite that of (i) .

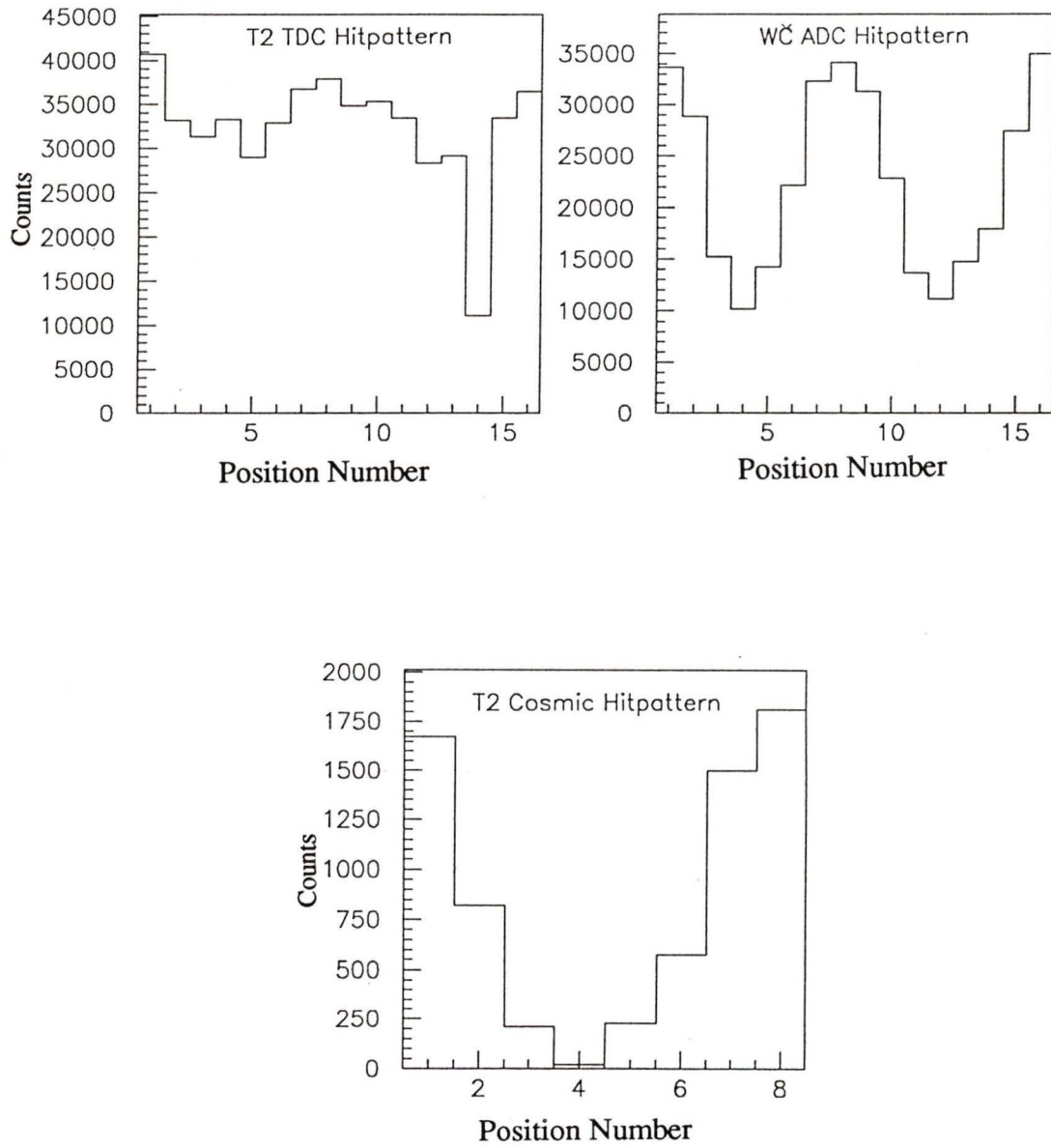


Figure 7.14: Hitpattern plots for the T2 and WČ arrays.

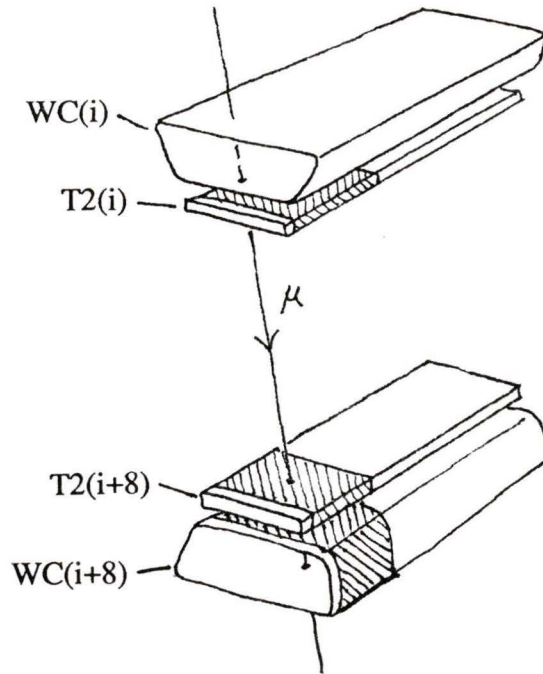


Figure 7.15: An illustration of the efficiency criteria.

$$\text{Efficiency}(i) = \frac{T2(i) * T2(i+8) * WC(i) * WC(i+8)}{T2(i) * T2(i+8) * WC(i+8)} \quad (7.1)$$

The calculated efficiencies are displayed graphically in Figure 7.17, and in numerical form in Table 7.1, which is generated automatically when histograms are saved after analyzing a data tape. The apparent anomalies of WC #4 and #12 can be attributed to poor statistics, as evident in the number of trials. Other than these cases, the detectors all seem to be functioning at a typical veto rate of 98% for leptons. Since the cosmic ray flux is predominantly downward, some cosmic rays may not trigger the bottom WC counter after losing energy or being stopped in the short distance between the bottom T2 and bottom WC. Therefore, there is a slight drop in efficiencies calculated by this method for WC counters near the bottom of the array, as is evident in Figure 7.17.

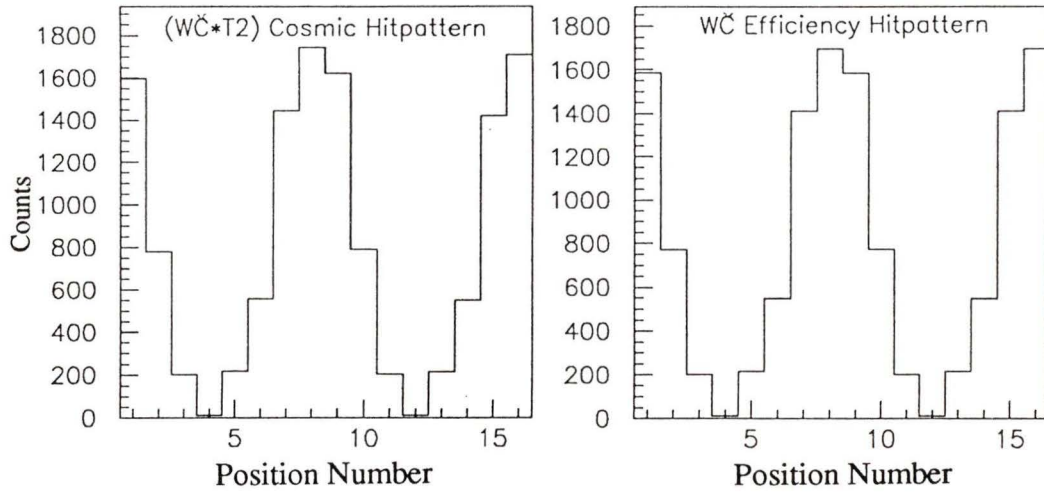


Figure 7.16: Hitpatterns involved in the overall efficiency calculation.

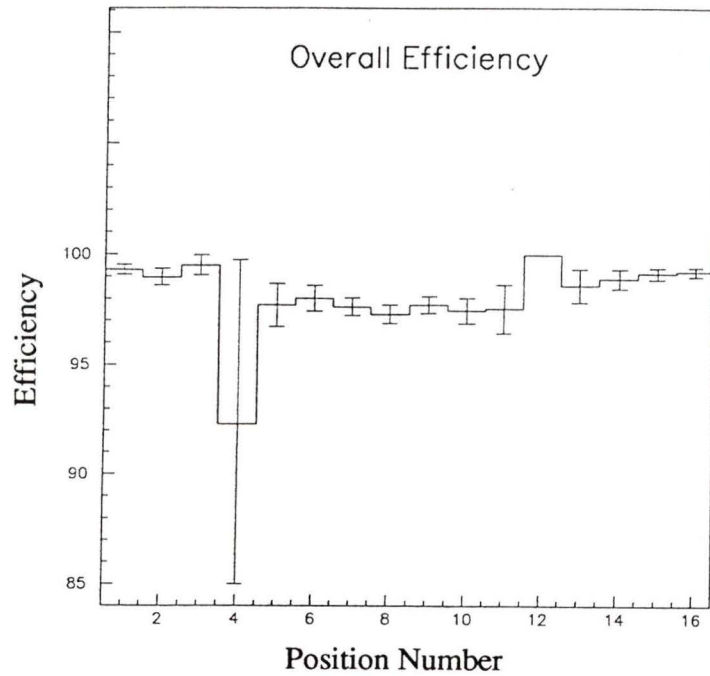


Figure 7.17: Veto efficiency calculated for each WC detector.

Table 7.1: Veto efficiency, standard deviation, and number of trials for each WC detector.

#	Efficiency	Dev.	Trials
1	99.31	0.21	1597
2	98.97	0.36	779
3	99.50	0.50	201
4	92.31	7.39	13
5	97.71	1.01	218
6	98.03	0.59	557
7	97.65	0.40	1445
8	97.31	0.39	1745
9	97.72	0.37	1623
10	97.47	0.56	791
11	97.56	1.08	205
12	100.00	0.00	12
13	98.61	0.80	216
14	98.91	0.44	552
15	99.16	0.24	1423
16	99.24	0.21	1711

The information of the cosmic track position provided by the T2 adjacent to each WC allows the calculation of an efficiency at a location along the length of the WC. The program of the Appendix further subdivides each WC into five zones of equal length, then displays a set of efficiency histograms using the same criteria as before, except that the WC must trigger in a zone determined by a hit in the adjacent T2. The result is displayed in Figure 7.18, with tabulated efficiencies shown in Tables 7.2 and 7.3. Again, the vertical tracks appear to be satisfactory, with anomalies in the horizontal tracks attributable to poor statistics in that direction. (Positions numbered #8 and #16 correspond to directly vertical tracks, while #4 and #12 correspond to directly horizontal tracks.)

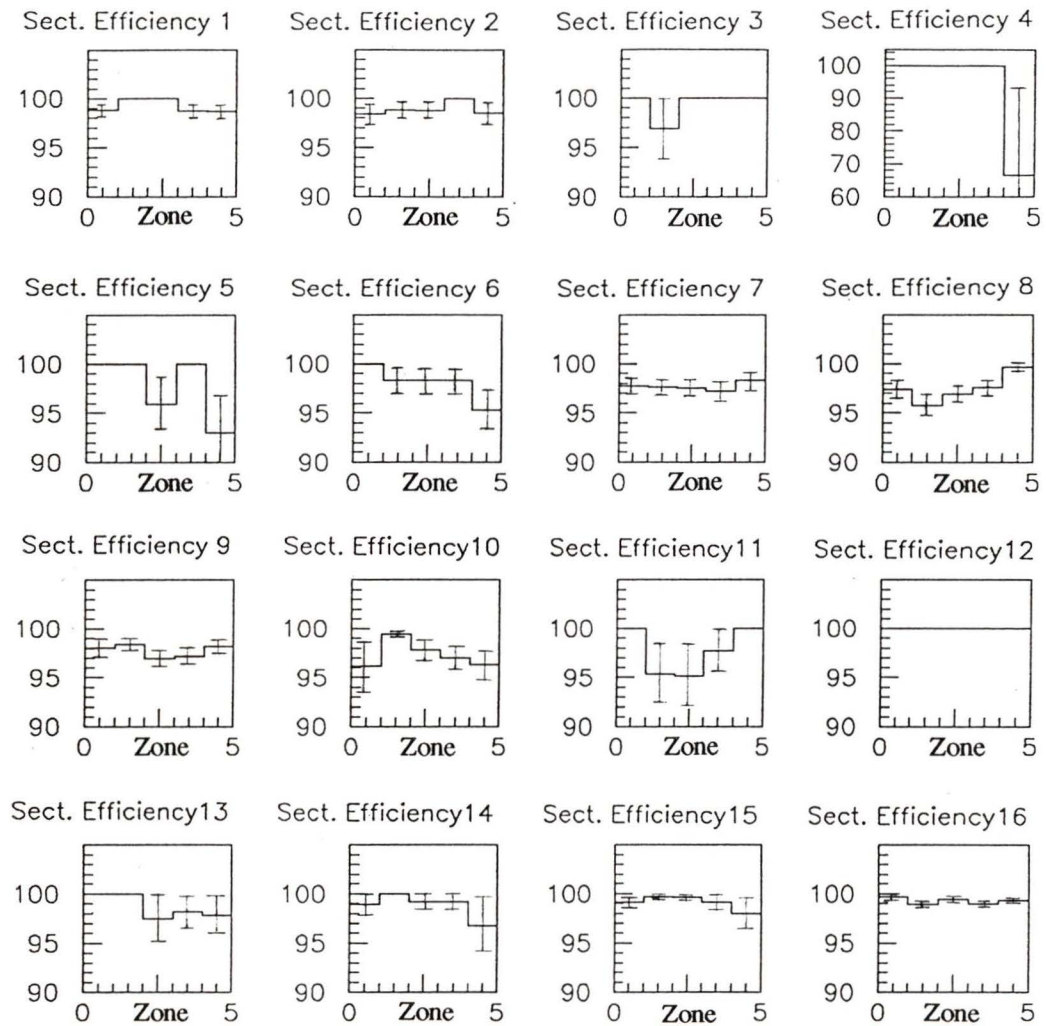


Figure 7.18: Sectional WC Veto efficiencies.

Table 7.2: Sectional veto efficiency, standard deviation, and number of trials for each WC detector (1 to 8).

# 1 Sectional Efficiency				# 5 Sectional Efficiency			
Zone	Efficiency	Dev.	Trials	Zone	Efficiency	Dev.	Trials
1	98.85	0.66	260	1	100.00	0.00	38
2	100.00	0.00	362	2	100.00	0.00	47
3	100.00	0.00	363	3	95.92	2.83	49
4	98.73	0.63	315	4	100.00	0.00	41
5	98.65	0.67	297	5	93.02	3.88	43

# 2 Sectional Efficiency				# 6 Sectional Efficiency			
Zone	Efficiency	Dev.	Trials	Zone	Efficiency	Dev.	Trials
1	98.39	1.13	124	1	100.00	0.00	98
2	98.84	0.82	172	2	98.29	1.20	117
3	98.76	0.87	161	3	98.31	1.19	118
4	100.00	0.00	190	4	98.31	1.19	118
5	98.48	1.06	132	5	95.28	2.06	106

# 3 Sectional Efficiency				# 7 Sectional Efficiency			
Zone	Efficiency	Dev.	Trials	Zone	Efficiency	Dev.	Trials
1	100.00	0.00	26	1	97.74	0.91	265
2	96.88	3.08	32	2	97.59	0.84	332
3	100.00	0.00	43	3	97.50	0.87	320
4	100.00	0.00	56	4	97.23	0.97	289
5	100.00	0.00	44	5	98.33	0.83	239

# 4 Sectional Efficiency				# 8 Sectional Efficiency			
Zone	Efficiency	Dev.	Trials	Zone	Efficiency	Dev.	Trials
1	100.00	0.00	3	1	97.39	0.91	306
2	100.00	0.00	1	2	95.79	1.00	404
3	100.00	0.00	3	3	96.91	0.88	388
4	100.00	0.00	3	4	97.57	0.80	370
5	66.67	27.22	3	5	99.64	0.36	277

Table 7.3: Sectional veto efficiency, standard deviation, and number of trials for each WC detector (9 to 16).

# 9 Sectional Efficiency				#13 Sectional Efficiency			
Zone	Efficiency	Dev.	Trials	Zone	Efficiency	Dev.	Trials
1	98.03	0.87	254	1	100.00	0.00	29
2	98.40	0.65	375	2	100.00	0.00	46
3	96.99	0.89	365	3	97.44	2.53	39
4	97.17	0.88	353	4	98.21	1.77	56
5	98.19	0.80	276	5	97.83	2.15	46

#10 Sectional Efficiency				#14 Sectional Efficiency			
Zone	Efficiency	Dev.	Trials	Zone	Efficiency	Dev.	Trials
1	96.15	1.69	130	1	98.94	1.06	94
2	99.43	0.57	174	2	100.00	0.00	121
3	97.81	1.08	183	3	99.17	0.82	121
4	97.02	1.31	168	4	99.19	0.80	124
5	96.32	1.61	136	5	96.74	1.85	92

#11 Sectional Efficiency				#15 Sectional Efficiency			
Zone	Efficiency	Dev.	Trials	Zone	Efficiency	Dev.	Trials
1	100.00	0.00	31	1	99.11	0.63	225
2	95.35	3.21	43	2	99.69	0.31	319
3	95.12	3.36	41	3	99.65	0.35	283
4	97.73	2.25	44	4	99.13	0.50	344
5	100.00	0.00	46	5	98.02	0.88	252

#12 Sectional Efficiency				#16 Sectional Efficiency			
Zone	Efficiency	Dev.	Trials	Zone	Efficiency	Dev.	Trials
1	100.00	0.00	2	1	99.65	0.35	289
2	100.00	0.00	1	2	98.90	0.55	364
3	100.00	0.00	2	3	99.45	0.39	361
4	100.00	0.00	4	4	98.98	0.51	392
5	100.00	0.00	3	5	99.34	0.46	305

In calculating the standard deviation of an efficiency, it is assumed that the number of counts recorded (N) is binomial in the number of trials (T) and in the probability of success (ρ) that a detector will register a count during any given trial. The variance of the efficiency (σ_E^2) is then given by

$$\sigma_E^2 = \frac{\sigma_N^2}{T^2} = \frac{T\rho(1-\rho)}{T^2} \quad (7.2)$$

The standard deviation σ_E is obtained by using the approximation

$$\rho = N/T \quad (7.3)$$

which is valid for large T . The standard deviation is then

$$\sigma_E = \sqrt{N/T^2(1-N/T)} \quad (7.4)$$

Chapter 8

Concluding Remarks

This work has presented the motivation and means for constructing a cylindrical array of sixteen water/umbelliferone Čerenkov detectors in an experiment to accurately measure the K-series X-ray lines of kaonic hydrogen.

The detector efficiencies have been gauged by their ability to discriminate between moderate-energy leptons, which are to be vetoed in the experiment, and pions with comparable momenta, which are not to be vetoed. Although the former efficiency has been shown to exceed 90%, there is some question as to the latter, which may exceed 10% in some instances. The overall effectiveness of this technique remains to be exhaustively tested, pending the outcome of the results for the entire experiment.

It should be mentioned, however, that modifications may be easily made to the design by draining the detectors and refilling them with a different solution, one of lower refractive index for example, if such an alteration is deemed necessary to lower the pion false veto rate. Alternatively, additional degrader may be added between the T2 and WČ arrays to further reduce the pion momenta.

Bibliography

- [1] J.D. Davies et al., Phys. Lett. **B83** 55 (1979).
- [2] M. Izycki et al., Z. Phys. **A297** 11 (1980).
- [3] P.M. Bird et al., Nucl. Phys. **A404** 482 (1983).
- [4] A.D. Martin, Nucl. Phys. **B179** 33 (1981).
- [5] R.H. Dalitz and J.G. McGinley, *Proceedings of the International Conference on Hypernuclear and Kaon Physics* (North Holland, Heidelberg 1982).
- [6] J.E. Conboy et al., J. Phys. G: Nucl. Phys **12** 1143 (1986).
- [7] E. Borie and M. Leon, Phys. Rev. **A21** 1460 (1980).
- [8] S. Deser, M.L. Goldberger, K. Baumann, W. Thirring, Phys. Rev. **96** 774 (1954).
- [9] R.H. Dalitz and S.F. Tuan, Ann. of Phys. **10** 307 (1960).
- [10] Y.-A. Chao et al., Nucl. Phys. **B56** 46 (1973).
- [11] J. Law et al., Phys. Rev. **C36** 2709 (1987).
- [12] K.S. Kumar and Y. Nogami, Phys. Rev. **D21** 1834 (1980).

- [13] K. Tanaka and A. Suzuki, *Phys. Rev.* **C45** 2068 (1992).
- [14] J. Schnick and R.H. Landau, *Phys. Rev. Lett.* **58** 1719 (1987).
- [15] L. Mallet, *C.R. L'Acad. des Sci. (Paris)* **183** 274 (1926).
- [16] P.A. Čerenkov, *C.R. L'Acad. des Sci. L'URSS (Doklady)*,
8, 451 (1934)
- [17] I.M. Frank and Ig. Tamm, *C.R. L'Acad. des Sci. L'URSS (Doklady)*,
14 109 (1937).
- [18] P. Nemethy et al., *Nucl. Inst. and Meth.* **173** 251 (1980).

Appendix

Program Listing

The following FORTRAN subroutines were used in gauging the efficiencies of the detectors using cosmic-rays, as described in chapter 7. The subroutines shown are part of a much larger collection of programs which decodes events from data tapes made at the KPX site. However, all the relevant logic for the histograms shown in chapter 7 are contained in these subroutines. The analysis was performed on 2.25×10^6 cosmic ray events gathered while the detector as a whole was not in use, at a time of 18 months after the Čerenkov detectors were filled and installed. Threshold levels for the WČ ADC triggers and T2 profile cutoffs must be set after examining the histograms from a first run of the program.

```

C-----C
C      C
C      File   Counters.for
C      C
C-----C

*****
      subroutine counters_define
*****
      character No*2

      call hbook1(100, 'T2 TDC Hitpattern', 16, 0.5, 16.5)
      call hbook1(110, 'WC ADC Hitpattern', 16, 0.5, 16.5)
      call hbook1(150, 'T2 TDC Multiplicity', 6, 0.5, 6.5)
      call hbook1(160, 'WC TDC Multiplicity', 8, 0.5, 8.5)
      call hbook1(420, 'T2 Cosmic Hitpattern', 8, 0.5, 8.5)
      call hbook1(430, '(WC*T2) Cosmic Hitpattern', 16, 0.5, 16.5)
      call hbook1(440, 'WC Efficiency Hitpattern', 16, 0.5, 16.5)
      call hbook1(510, 'Overall Efficiency', 16, 0.5, 16.5)
      Do j = 1, 16
         write(No,'(i2)') j
         call hbook1(200+j, 'T2 '//No//' up   TDC', 300, 0., 3000.)
         call hbook1(220+j, 'T2 '//No//' down TDC', 300, 0., 3000.)
         call hbook1(240+j, 'T2 up - T2 down '//No//' ', 200, 0., 2000.)
         call hbook1(300+j, 'WC '//No//' TDC', 500, 0., 2000.)
         call hbook1(320+j, 'WC '//No//' ADC', 410, 0., 4100.)
         call hbook1(520+j, 'Sect. Eff. Denominator '//No//' ', 5, 0., 5.)
         call hbook1(540+j, 'Sect. Eff. Numerator '//No//' ', 5, 0., 5.)
         call hbook1(600+j, 'Sect. Efficiency '//No//' ', 5, 0., 5.)
      EndDo
      return
      end

*****
      subroutine counters(T, WC)
*****
      include '[spinor.thesis]tapebuff.inc'

ccc   DATA PASSED HERE AS:
c     T(T1=1/T2=2,Upstream=1/Downstream=2,#1-#16,ADC=1/TDC=2)
ccc   WC(#1-#16,ADC=1/TDC=2)

      integer ADC/1/, TDC/2/, UP/1/, DOWN/2/
      real T(2,2,16,2), WC(16,2)

      real wcth(16)
ccc   WC ADC THRESHOLDS MUST BE SET FROM RAW HISTOGRAMS (320+j)
      data wcth/250.,250.,320.,320.,
&          370.,370.,200.,210.,
&          110.,250.,250.,190.,
&          200.,200.,320.,310./

      real T2L(16), T2H(16), T2dif(16)
ccc   T2 PROFILE LIMITS DEPEND UPON CABLE LENGTHS AND MUST
ccc   BE SET FROM HISTOGRAMS OF T2dif
      data T2L/889.,788.,788.,868.,
&          847.,876.,817.,674.,
&          716.,935.,813.,725.,
&          910.,947.,859.,1082./
      data T2H/1145.,1027.,1040.,1120.,
&          1099.,1111.,1069.,922.,
&          969.,1179.,1069.,973.,
&          1170.,1200.,1107.,1317./

```

```

logical Hit(3,16), Cosmic(2,8)
integer Mult(3)
integer T1/1/, T2/2/, W/3/

real zone(16)

**** Establish hitpatterns and multiplicities
ccc   Clear counters
      Do j = 1, 3
        Mult(j) = 0
        Do k = 1, 16
          Hit(j,k) = .false.
        EndDo
      EndDo
      Do j = 1, 2
        Do k = 1, 8
          Cosmic(j,k) = .false.
        EndDo
      EndDo

ccc   Fill counters
      Do j = 1, 16
        if(T(T2,UP,j,TDC) .gt. 1.) call hF1(200+j,T(2,1,j,2),1.)
        if(T(T2,DOWN,j,TDC) .gt. 1.) call hF1(220+j,T(2,2,j,2),1.)
        If(T(2,1,j,2) .gt. 1. .and. T(2,2,j,2) .gt. 1. .and.
1      T(2,1,j,2) .lt. 1800. .and. T(2,2,j,2) .lt. 1800.) then
          T2dif(j) = T(T2,UP,j,TDC) - T(T2,DOWN,j,TDC) + 1000.
          call hF1(240+j,T2dif(j),1.)
          If (T2dif(j) .gt. T2L(j) .and.
1      T2dif(j) .lt. T2H(j)) then
            Hit(T2,j) = .true.
            Call hF1(100,real(j),1.)
            Mult(T2) = Mult(T2) + 1
          Endif
        Endif

        Call hF1(300+j,WC(j,2),1.)
        Call hF1(320+j,WC(j,1),1.)
        If (WC(j,ADC) .gt. wcth(j)) then
          Call hF1(110,real(j),1.)
          Hit(W,j) = .true.
          Mult(W) = Mult(W) + 1
        Endif
      EndDo
      Call hF1(150,real(Mult(T2)),1.)
      Call hF1(160,real(Mult(W)),1.)

**** Cosmic Filters & General Efficiency Preview
      If(Mult(T2) .eq. 2) then
        Do j = 1, 8
          If(Hit(T2,j) .eq. .true. .and. Hit(T2,(j+8)) .eq. .true.) then
            Cosmic(T2,j) = .true.
            Call hF1(420,real(j),1.)
            If (Hit(W,j) .eq. .true.) then
              Call hF1(430,real(j+8),1.)
              If (Hit(W,j+8) .eq. .true.) then
                Call hF1(440,real(j+8),1.)
              Endif
            Endif
          If (Hit(W,(j+8)) .eq. .true.) then
            Call hF1(430,real(j),1.)
            If (Hit(W,j) .eq. .true.) then
              Call hF1(440,real(j),1.)
            Endif
          Endif
        EndDo
      Endif
      Endif

```

```

**** Sectional Efficiencies
  Do j = 1, 8
    If(Cosmic(T2,j) .eq. .true.) then
      Zone(j)=(T2dif(j)-T2L(j))*5./(T2H(j)-T2L(j))
      Zone(j+8)=(T2dif(j+8)-T2L(j+8))*5./(T2H(j+8)-T2L(j+8))
      If(Hit(W,j) .eq. .true.) then
        Call hFl(520+j+8,Zone(j+8),1.)
        If(Hit(W,(j+8)) .eq. .true.) then
          Call hFl(540+j+8,Zone(j+8),1.)
        Endif
      Endif
      If(Hit(W,(j+8)) .eq. .true.) then
        Call hFl(520+j,Zone(j),1.)
        If(Hit(W,j) .eq. .true.) then
          Call hFl(540+j,Zone(j),1.)
        Endif
      Endif
    Endif
  EndDo

  Return
  End

*****
  subroutine counters_efficiency
  *****
  c      This subroutine is called by Molli.for
  c      after receiving 'save' command
  ccccccccccccccccccccccccccccccccccccccccccccccccccccccccc
  real num(16,6), den(16,6), dev(16,6), eff(16,6)

  open (unit=9, file='efficiency', status='new')

  Write(9,*)' # Efficiency Dev. Trials'
  Write(9,*)' -----'
  Do j = 1, 16
    num(j,6) = hx(440,real(j))
    den(j,6) = hx(430,real(j))
    If(den(j,6) .ne. 0.) then
      eff(j,6) = 100.*(num(j,6))/den(j,6)
      Call hFl(510,real(j),eff(j,6))
    dev(j,6) = 100.*SQRT((num(j,6)/(den(j,6)**2.))*(1.-num(j,6)/den(j,6)))
    Write(9,900)j, eff(j,6), dev(j,6), int(den(j,6))
    Endif
  EndDo

  Do j = 1, 16
    Write(9,*)' '
    Write(9,910)j
    Write(9,*)' Zone Efficiency Dev. Trials'
    Write(9,*)' -----'
    Do k = 1, 5
      num(j,k) = hx(540+j,(real(k)-0.5))
      den(j,k) = hx(520+j,(real(k)-0.5))
      If(den(j,k) .ne. 0.)then
        eff(j,k) = 100.*num(j,k)/den(j,k)
        Call hFl(600+j,real(k-1),eff(j,k))
      dev(j,k)=100.*SQRT((num(j,k)/(den(j,k)**2.))*(1.-num(j,k)/den(j,k)))
      Write(9,905)k, eff(j,k), dev(j,k), int(den(j,k))
      Endif
    EndDo
  EndDo

900  Format(I3,' ',F6.2,' ',F6.2,' ',I7)
905  Format(I3,' ',F6.2,' ',F6.2,' ',I7)
910  Format(' #',I2,' Sectional Efficiency')

  Return
  End

```

Vita

Surname: Trayling
Given Names: Gregory James
Place of Birth: Vancouver, British Columbia, Canada
Date of Birth: 1st of December, 1963

Educational Institutions Attended:

University of Victoria, Canada	1991-1994
Simon Fraser University, Canada	1981-1991

Degrees Awarded:

B.Sc. Hons. (Physics major, Nuclear Science minor)	1991
--	------

Honours and Awards:

1st Prize, Canadian Undergraduate Physics Conference, Laval (Best scientific paper presentation)	1990
---	------

Publications:

"Temperature Dependence of the Landau-Lifshitz Damping Parameter for Iron", J.F. Cochran, J.M. Rudd, W.B. Muir, G. Trayling, and B. Heinrich, *J. Appl. Phys.* **70** (10), 1991.

"Kaonic Hydrogen X-ray Experiment at KEK", M. Iwasaki, G. Trayling et al, *Proceedings of the International Conference on Hypernuclear and Strange Particle Physics* (to be published, Vancouver 1994).

Partial Copyright License

I hereby grant the right to lend my thesis to users of the University of Victoria Library, and to make single copies only for such users, or in response to a request from the library of any other university or similar institution, on its behalf or for one of its users. I further agree that permission for extensive copying of this thesis for scholarly purposes may be granted by myself or a member of the university designated by me. It is understood that copying or publication of this thesis for financial gain shall not be allowed without my written permission.

Title of Thesis:

The Design and Construction of a Discriminating Čerenkov Veto Counter Array

Author: Gregory James Trayling



Sept 30, 1994

(Date)